BRNO UNIVERSITY OF TECHNOLOGY

VYSOKÉ UČENÍ TECHNICKÉ V BRNĚ

FACULTY OF MECHANICAL ENGINEERING

FAKULTA STROJNÍHO INŽENÝRSTVÍ

ENERGY INSTITUTE

ENERGETICKÝ ÚSTAV

ANALYSIS OF INHALED PARTICLES DEPOSITION IN A MODEL OF HUMAN LUNGS

ANALÝZA USAZOVÁNÍ INHALOVANÝCH ČÁSTIC V MODELU LIDSKÝCH PLIC

BACHELOR'S THESIS

BAKALÁŘSKÁ PRÁCE

AUTHOR — Adam Miček

AUTOR PRÁCE

SUPERVISOR — Ing. František Lízal, Ph.D.

VEDOUCÍ PRÁCE

BRNO 2017

VYSOKÉ UČENÍ TECHNICKÉ V BRNĚ
FAKULTA STROJNÍHO INŽENÝRSTVÍ

Zadání bakalářské práce

Ústav:	Energetický ústav
Student:	**Adam Miček**
Studijní program:	Strojírenství
Studijní obor:	Základy strojního inženýrství
Vedoucí práce:	**Ing. František Lízal, Ph.D.**
Akademický rok:	2016/17

Ředitel ústavu Vám v souladu se zákonem č.111/1998 o vysokých školách a se Studijním a zkušebním řádem VUT v Brně určuje následující téma bakalářské práce:

Analýza usazování inhalovaných částic v modelu lidských plic

Stručná charakteristika problematiky úkolu:

Student provede vyhodnocení množství usazených částic v jednotlivých oblastech plic. Inhalované částice byly značeny radioaktivní látkou a jejich množství bylo měřeno pomocí pozitronové emisní tomografie. Student provede zpracování obrazů z tomografu pomocí software Carimas a vyhodnotí vliv velikosti částic a rychlosti nádechu na osud vdechnutých částic.

Cíle bakalářské práce:

– Provést rešerši dostupných experimentálních metod pro měření regionální depozice inhalovaných částic zejména v in vitro modelech plic a zhodnotit jejich výhody a nevýhody.
– Zpracovat a uspořádat data z měření depozice částic pomocí pozitronové emisní tomografie.
– Vyhodnotit objemové radioaktivity v jednotlivých částech modelu plic pro různé průtoky a různé velikosti inhalovaných částic.
– Vypočítat depoziční charakteristiky (např. depoziční frakci a účinnost) a porovnat výsledky s dříve publikovanými experimenty.

Seznam doporučené literatury:

LÍZAL F. Experimentální výzkum transportu a depozice aerosolů v dýchacím traktu člověka. Dizertační práce. Brno: Vysoké učení technické v Brně, Fakulta strojního inženýrství, 2012. 137 s.

CONWAY J. Lung imaging - Two dimensional gamma scintigraphy, SPECT, CT and PET. Advanced Drug Delivery Reviews. 2012; 64: 357-68.

SAHA G. B. Basics of PET imaging physics, chemistry, and regulations. 2nd ed. New York; London: Springer, 2010.

Termín odevzdání bakalářské práce je stanoven časovým plánem akademického roku 2016/17

V Brně, dne

L. S.

doc. Ing. Jiří Pospíšil, Ph.D. ředitel ústavu	doc. Ing. Jaroslav Katolický, Ph.D. děkan fakulty

Acknowledgments

I am greatly thankful to my supervisor Ing.František Lízal, Ph.D. for his kind support and guidance which led me to successful completion of my thesis. Further, I would like to thank my family, for the support they have provided me throughout my entire life, their great patience and love.

Affirmation

I declare that this bachelor thesis is result of my own work, led by my supervisor, and all used sources are duly listed in bibliography. I proclaim that all presented information is true and valid to the best of my knowledge.

Adam Miček

Bibliographic citation

MIČEK, A. *Analýza usazování inhalovaných částic v modelu lidských plic*. Brno: Vysoké učení technické v Brně, Fakulta strojního inženýrství, 2017. 58 s. Vedoucí bakalářské Ing. František Lízal, Ph.D.

Abstract

Correct understanding of aerosol deposition and behavior in human respiratory tract is crucial for the efficient delivery of medication and health protection. This bachelor thesis analyses deposition of 1μm particles in realistic and idealized lung geometry, from data previously acquired by positron emission tomography (PET) and computed tomography (CT).

PET and CT scans were imported into Carimas 2.0 software which was used to obtain value of volumetric radioactivity. Corrections were applied to the acquired values and consequently, deposition characteristics were calculated and reviewed. Data was also compared to previous studies.

Methodology of analyses and calculations was validated by duplicity of scans and their analyses, and repetition of analyses by another trained person which confirmed its good stability and credibility of use. Described procedure can serve as an example of possible way to process PET and CT data in Carimas software. Obtained detailed information about deposition and numerous deposition characteristics can be used for comparison in future studies, experiments, or used as data for validation of computer modeled deposition. Based on deposition results, inertial impaction was confirmed to be the dominant deposition mechanism in realistic model of lungs and very little impact of flow rate on deposition was found for idealized model of lungs.

Keywords

Aerosol, aerosol deposition, deposition analysis, inhaled particles, model of lungs

Abstrakt

Správne pochopenie depozície aerosólu a jeho správania v dýchacích cestách človeka je nevyhnutné pre zabezpečenie efektívneho podávania medikamentov a ochranu zdravia. Táto bakalárska práca analyzuje usadzovanie 1 μm častíc, v realistickom a idealizovanom modely pľúc na základe dát získaných pozitrónovou emisnou tomografiou (PET) a počítačovou tomografiou (CT).

Dáta z PET a CT skenerov boli nahrané do softvéru Carimas 2.0, ktorý bol použitý na získanie hodnôt objemovej rádioaktivity. Získané hodnoty boli skorigované a následne boli vypočítané depozičné charakteristiky. Výsledky boli okomentované a porovnané s predchádzajúcimi štúdiami.

Vhodnosť spôsobu analýzy a výpočtov bola kontrolovaná opakovanou analýzou dát a taktiež zopakovaním celého postupu analýzy nezávislou zaškolenou osobou, čím bola potvrdená stabilita a vhodnosť tejto metódy. Popísaný postup môže slúžiť ako podpora pri spracovávaní PET a CT skenov v programe Carimas. Podrobné informácie o depozícii a niekoľko depozičných charakteristík môžu slúžiť pre porovnania s budúcimi štúdiami, experimentmi alebo môžu byť použité pri validácii dát pre počítačom modelovanú depozíciu. Na základe výsledkov môžeme tvrdiť, že hlavným depozičným mechanizmom pre realistický model pľúc je zotrvačný mechanizmus a zmena prietoku aerosólu idealizovaným modelom má len veľmi malý vplyv na depozíciu.

Kľúčové slová

Aerosól, depozícia aerosólu, analýza depozície, inhalované častice, model pľúc

Contents

1 Introduction

Deposition of particles in human airways has always been a complex topic. However, understanding of particle deposition is inevitable for using lung as a route for delivery of aerosolized medication and to ensure sufficient protection from toxic particles. One of the obstacles on the way to understand what really happens and how to make particles deposit in specific place, is an extreme complexity of human lungs. It is one of the most complicated organs in human body, composed of 300-500 million alveoli and surface area of 100 m^2. On the other hand, large absorptive surface allowing high absorption rates makes it an organ of interest for continuous studies. Its potential lies in the possibility of easy, quick, cheap, comfortable (e.g. needle-free) and effective treatment. Not only could it be used to treat respiratory tract connected diseases, but also to deliver a systemic effect of therapeutic aerosols which brings relief from other health issues (Nahar *et al.*, 2013). Because the cure for different types of diseases requires drug particles to deposit in different regions of lungs, the key factor to effective treatment is localized aerosol delivery. Possibility to control the amount and area of deposited medication is essential in the pursuit of optimal and safe treatment (Cheng, 2014). Intricate relationship between particle size, density, inhalation regime and inter-subject structural configuration determines the amount and place of deposition (Grgic *et al.*, 2004). There are five mechanisms by which deposition in lung can occurs: inertial impaction, sedimentation, diffusion, interception and electrostatic precipitation. Inertial impaction, sedimentation, diffusion are the leading causes of deposition (Figure 1). The purpose of this bachelor thesis is to analyze data of deposition in model of human lungs which has been acquired by positron emission tomography (PET) and provide additional information for better understanding of particle deposition in human lungs.

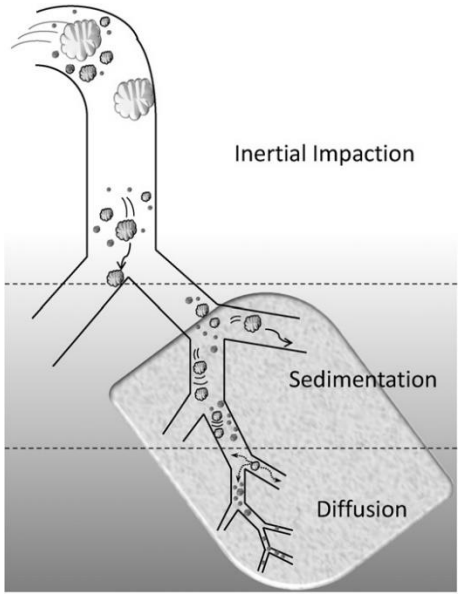

Figure 1: Main deposition mechanism in human lungs related to particle size. Smaller particles tend to deposit generally by diffusion in lower part of respiratory tract, while bigger particles deposit mainly by inertial impaction in larger airway. Gastrointestinal tract is omitted in the diagram (Carvalho et al., 2011).

2 Radionuclide imaging

2.1 Gamma scintigraphy

The first gamma camera was invented and used by Hal Anger, an electrical engineer from California around 60 years ago (Wagner, 2003). Since then, gamma scintigraphy has been used up to date. It has been extensively used for distribution and delivery efficiency studies. Usually, the process of radiolabeling involves adding radionuclide to the solution used for the experiment. The most frequently used radionuclide for this type imaging is Technetium (99mTc, half-life of 6 h). It has wide application in nuclear medicine for diagnostic testing. Other alternatives include Indium (111In, half-life of 68 h) and, very rarely, Iodine (123I, half-life of 13.3 h). These radionuclides are mostly used for in vivo experiments when the long-term deposition and clearance is tested (Conway, 2012).

The images in gamma scintigraphy are provided by single-headed or dual-headed gamma cameras (Figure 2). Produced images can deliver relevant information about the distribution of the radiolabeling agent in the organ of interest. It is very common to divide lungs into sections of interest and to determine the specific region, in which the particles have deposited. This is done by computer programs (Carvalho *et al.*, 2011). However, a number of different algorithms may be used to determine the regional distribution of the drug which requires dividing model between 2 to 10 regions. The size and shape of regions of interest shows a considerable variation between laboratories. These variations cause a major problem in comparing data, which is one of the first drawbacks of the gamma scintigraphy (Scheuch *et al.*, 2010). Another problem occurs with a projection of 3D structure into 2D image. This may cause an overestimation of the deposition due to overlapping airways (Carvalho *et al.*, 2011). Investigation of the methods for extracting 3D information from 2D data had been made but has not yet been fully implemented into use (Scheuch *et al.*, 2010).

Figure 2:Single-headed gamma camera (Ergo, 2011).

Gamma scintigraphy has large body of literature in the deposition studies and is the mainstay for the in vivo determination of lung deposition. Despite its wide use, its usefulness is strictly limited. The only advantage that can be taken into consideration when talking about this method is its simplicity. Gamma scintigraphy has lost a good deal of importance in the last decade (Berridge *et al.*, 2003). Therefore, the methods such as single photon emission computed tomography (SPECT) and PET are being used to overcome errors caused by planar imaging of 3D structures increasingly nowadays (Carvalho *et al.*, 2011).

2.2 Single photon emission computed tomography

The information provided by Gamma scintigraphy is significantly limited due to fact that the outcome is only 2D. Therefore, SPECT is used to overcome this problem and provide more reliable information because the deposition is not viewed as compressed 2D image. Contrary to the planar sections which are based on pixels, 3D structure is divided into volumes of interest (voxel) (Carvalho *et al.*, 2011). Using the same radiolabeling method as Gamma scintigraphy, commonly used radionuclide is also the same. 99mTc is suitable because it provides stable activity during the scanning and is only very slowly absorbed (Scheuch *et al.*, 2010).

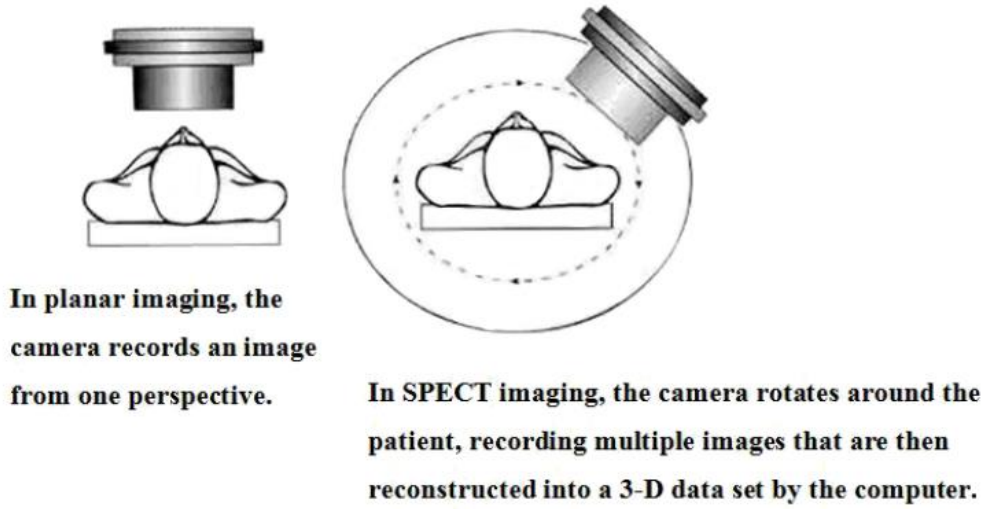

Figure 3:Comparison of planar imaging and SPECT (Researchgate, 2004).

In SPECT, unlike in gamma scintigraphy, the camera is not taking interior and posterior pictures but rotates around the subject at 360° and collects data (Figure 3). The pictures are then processed and converted into 3D structure (Nahar *et al.*, 2013). However, this process takes time, which can be sometimes longer than acceptable (more than 15 min). Therefore twin-headed or triple-headed cameras have been used to shorten the time of scanning and minimize the impact of absorption and clearance (Carvalho *et al.*, 2011). Advantages of the usage of multi-headed SPECT cameras include the increased sensitivity of the system and the possibility of reducing amount of radiation (in half when using a dual-headed camera) (Newman and Wilding, 1999). However, the statistical quality of quickly acquired data by multi-headed SPECT cameras is limited (Conway, 2012).

The main part of the SPECT system consists of detectors. They collect the high-energy photons emitted by radiolabeled object, estimate the photon energy, its location and provide the data for image reconstruction. There are different types of such detectors. Scintillation camera i.e. anger camera, consisting of single crystal. Scintillation crystals i.e. pixelated camera as opposed to the previous example uses a large number of crystals, therefore more compact design of detector can be achieved. High counting rates can be perceived by this detector, but there is possibility of degrading an energy resolution. Different SPECT system has been introduced lately, using a semiconductor/solid-state detector. Main advantage is improved count sensitivity, energy resolution and spatial resolution (Holly *et al.*, 2010).

For the reconstruction of SPECT image, it is not only important to detect as many photons as possible but also to acquire an incident direction of each count. The external collimator is used for this purpose. Only a specific direction or a small range of directions is detected. Emitted photons which are outside the range of incident angles are absorbed by collimator (
Figure *4*). By restricting the number of photons and shortening the range of incident angles, it is possible to obtain higher resolution but at the expense of sensitivity. This resolution versus sensitivity trade-off is making collimator significantly affect image quality. Examples of

collimators used in SPECT systems include: parallel-hole collimator, sweeping parallel-hole collimator, converging collimator, multi-pinhole collimator and others. Collimators and detectors are then attached to the gantry which rotates the anger cameras and combined with other components, create the whole SPECT system (Holly *et al.*, 2010).

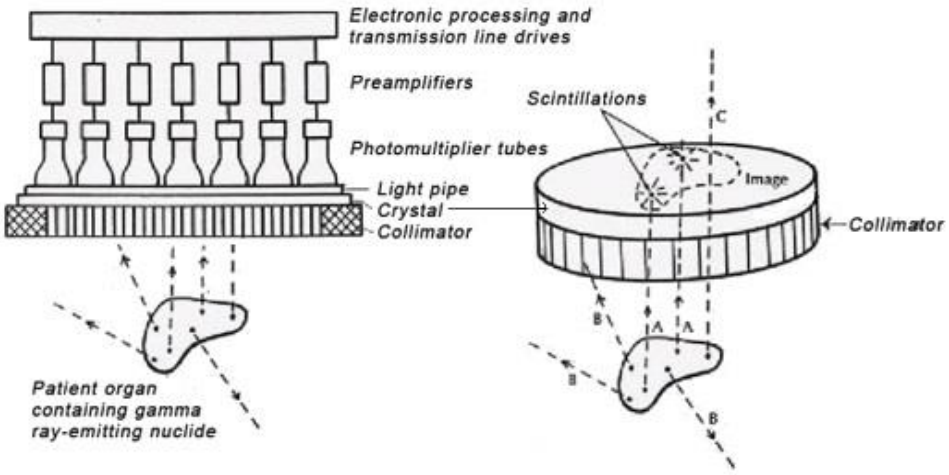

Figure 4 : Acquisition of SPECT data. Only photons with required directions pass the collimator (Scielo, 2005).

SPECT has been recently used for multimodal imaging. In the past, prior to SPECT images, anatomical images had to be obtained by CT or MRI, which were not part of a SPECT scanner. Images had to be aligned with those acquired by SPECT, in order to be used. Nowadays, combined SPECT-CT scanners (Figure 5) have become more common, allowing the scans to be obtained without moving of the subject or model and improving their alignment. (Fleming *et al.*, 2011).

Figure 5 : Combined SPECT-CT scanner (Ge Healthcare, 2004).

Advantages of SPECT over planar imaging are indubitable. Unfortunately, SPECT also carries some disadvantages. In the past, SPECT brought longer imaging times, larger amounts of

radiotracer, higher price level and more difficult analysis, compared to gamma scintigraphy (Newman and Wilding, 1999). Though, there has been a significant change in recent years. Number of SPECT scanners is higher than number of planar devices, scanning-time is being reduced, SPECT can be done sometimes more easily than planar study and information provided is qualitatively and quantitatively improved. It is technological progress, what is making SPECT more available, cheaper and producing more relevant data in shorter time (Berridge *et al.*, 2003).

2.3 Positron emission tomography

Positron emission tomography (PET) is becoming a commonly used imaging tool in nuclear medicine nowadays. Its main use is in clinical oncology, mostly to monitor the treatment and staging of cancer over time. The scanning agent concentrates in metabolically hyperactive tissue e.g. tumors and inflamed areas, therefore these areas can be identified. PET has been used for monitoring processes in lungs, including blood flow, drug metabolism, particle deposition, regional distribution etc. (Scheuch *et al.*, 2010). It is also possible to use this imaging method for gathering information about particle deposition in models of human lungs (Lizal *et al.*, 2012).

PET method requires labeling of the drug with positron-emitting isotope. These mostly include 11C, 13N, 15O, 18F, and 64Cu and their half-lives vary from 2 min up to 12.7 h. (Scheuch *et al.*, 2010). After the decay of chosen radio-isotope, the positrons are emitted and produce two high-energy photons by annihilating with electrons. Photons are propagating simultaneously, at approximately 180° to each other. These photons are detected and an event is recorded (Figure 6). Sum of such events then results in approximate quantities of the radio-isotope distribution (Nahar *et al.*, 2013). Detection of this event is made by PET scanner. The scanner consists of an array of detectors in the shape of the ring which surrounds the area of detection. Avoiding of lead collimation in the detector results in possibility of detecting picomolar concentration of the radiolabeled drugs because of high sensitivity. Afterward a 3D deposition representation can be build up by suitable software (Ollinger and Fessler, 1997).

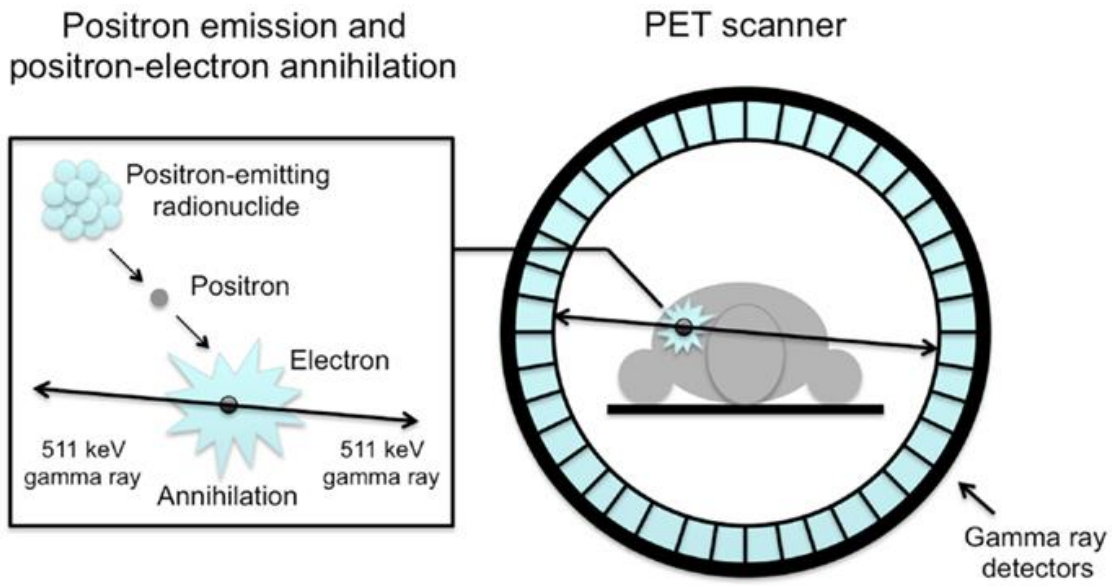

Figure 6: Principle of PET imaging and scheme of PET scanner (Frontiers, 2013).

While the SPECT and gamma scintigraphy uses surrogate markers to radiolabel the formulation, PET is functional imaging method which chemically incorporates the radiolabels into drug molecule. It can be used to provide information about bio distribution and in vivo pharmacokinetics. It can also be used to monitor the clearance and changes in distribution which is a strong advantage of the PET, because such data is hard or impossible to acquire by SPECT or other imaging methods (Berridge *et al.*, 2003). The short half-life of applied radionuclide allows a greater amount to be used and shortens the time of scanning. On the other hand, use of radionuclide leads to some disadvantages. The short half-life creates a necessity to have cyclotron close by, due to quickly decaying radiotracer which causes a time pressure. The another disadvantage is complicated use, complex radiolabeling and the running and capital costs, by far higher than the costs of planar imaging or SPECT (Newman and Wilding, 1999). Another issue appears when talking about comparing and validation of the data. Hence, more laboratories should use this method, so that fundamental questions connected to the clearance and deposition can be answered (Scheuch *et al.*, 2010).

There has been a significant progress in multimodal PET-CT and PET-MRI imaging lately. PET and CT imaging which is done simultaneously, can be a source of precise information about accumulation of radiotracer. The advantage of PET-CT and PET-MRI is the fact that the radiation dose is reduced. There has not only been progress in implementing multimodal imaging, but also the way of combining PET and CT or MRI scanners has experienced technical improvements (Park *et al.*, 2012). Two imaging devices mounted in series are used for PET-CT scanner. First, a CT scanner is used, promptly followed by a moving the object or the body to the PET gantry (Venegas *et al.*, 2013). There are several possibilities in mounting and combination of PET-MRI systems. PET scanner (Figure 7) can be either put inside the MRI scanner or inserted between MRI gradient coils. Other approach can be e.g. rotating subject holder, which transports the subject between standard system of PET and MRI scanners to obtain the required data.

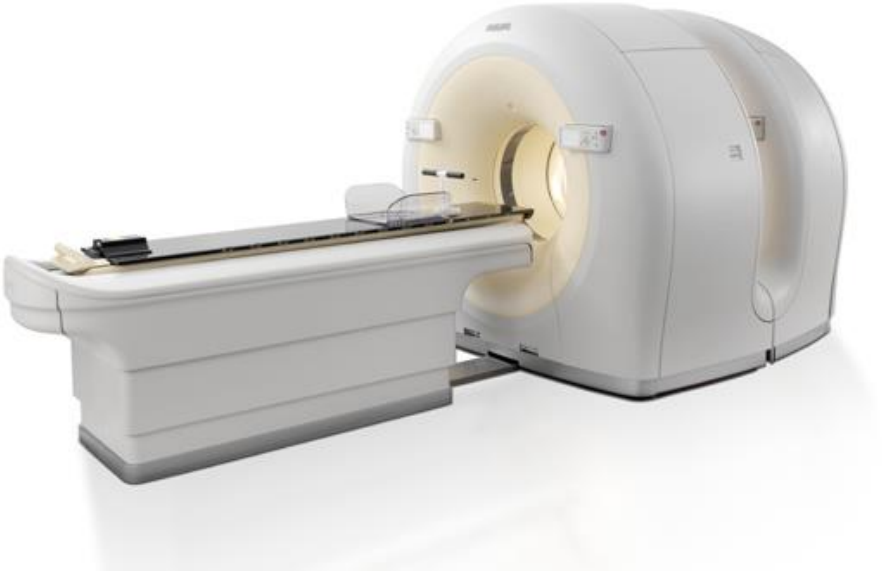

Figure 7: PET scanner (Phillips, 2008).

3 Optical imaging

3.1 Phase contrast optical microscopy

Phase contrast optical microscopy (PCOM) is typically used for monitoring airborne fiber concentrations and deposition in respiratory tract (Who, 1997). Even though, fibers are usually the particles of interest for this method, it can also be used for other types of particles e.g. spherical particles. (Belka *et al.*, 2014)

Membrane filter method is the recommended method for the use of PCOM, mostly because of the possibility to compare the results from different laboratories. However, differences easily occur due to systematic and random components, such as alterations in sample preparation, optical microscopy, calculations and mainly by the microscopist who analyses the samples and counts the fibers. These can only be eliminated by implementing standard procedures and formation of reproducible routine.

For this method, a fiber which should be taken into consideration during counting, is defined as object with a length longer than 5 μm, a width shorter than 3 μm and a length to width ratio larger than 3: 1. The PCOM method is limited when the samples contain flat or needle-shaped particles and there is not enough knowledge about the atmosphere where the sampling took place. It is also not possible to use this method to distinguish between different fiber types, because it does not provide data about chemical composition or crystallographic structure of fibers. Other methods described later can be used to provide supplementary information on size or type of fiber.

There are recommended specifications for some parameters which are crucial for the comparing of the acquired data. For example, size of the pores in the filters should not be too small to cause an obstruction for the pump and yet not too big to let the fibers fly trough. Using filter with grid can help in the position identification and can be an indicator of an error in filter mounting when distorted. Filters used in the experiment should undergo a minimal exposure to the environment outside of the experimental setup and therefore, should be opened directly before the use and sealed immediately afterwards. Crushing and vibration should be eliminated during the transport and storage. Contamination should be minimized by use of clean holders, cowls, areas with no fiber contamination and importantly, during the whole experiment filters should be handled with special care.

It is important to ensure that the density of fibers deposited on the filters stays approximately in the range from 100 to 650 fibers/ mm^2. The upper and lower limits may be extended but it is necessary to take into consideration the fact that the counts for high densities usually become underestimated and for low densities overestimated. The correct fiber density is achieved by adjusting flow rate, sampling time or filter diameter.

Preparation of the filters for evaluation requires exposure of the filter to acetone vapors, subsequent condensation leads to collapse of the filter pores and the filter becomes transparent. It is then mounted to a glass slide and contrast liquid is added.

Because this method is based on optical microscopy its crucial to use the correctly set microscope. Firstly, to provide most accurate information about the number of fibers and secondly to allow interlaboratory validation. To achieve good counting results G-22 Walton-Becket graticule (Figure 8) is specially designed for this purpose. It defines the area of interest in which the fibers are counted and provides reference image and dimension scales for sizing the fibers.

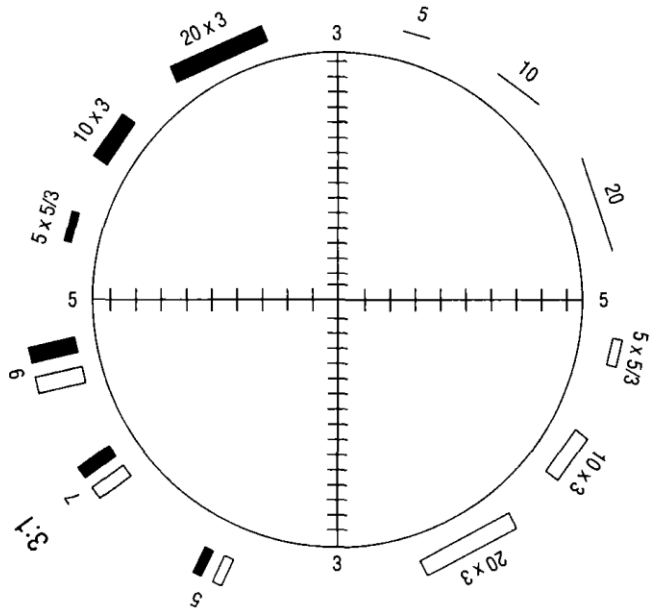

Figure 8: Walton-Becket graticule (Who, 1997).

One of important factors when choosing the best method for evaluation of particle deposition, concentration or any other factor is accuracy. However, for this method, accuracy cannot be assessed because the "true" fiber concentration of given dust cloud is not known. Though, the goal is to provide the most relevant output data. It can be achieved by reduction in statistical, systematic and subjective variations. The data acquired by membrane filter method are reliable only when the points of quality assurance program have been properly followed (Who, 1997).

Manual counting and subjective errors caused by the microscopist can be overcome by a novel approach implemented into PCOM. Filters are imaged in gray scale with high resolution camera connected to the microscope with phase contrast. The manual counting is then substituted by the use of novel software. In order for the software to identify and count the fibers correctly, images have to undergo analyses consisting of six main steps mostly to enhance the contrast and remove non-fiber objects. Although, the most important task is to keep quality and purity of the filters at the highest possible level, because the software cannot distinguish fibers from other objects, and in the case of low quality, the traditional method of manual counting needs to be performed (Lizal *et al.*, 2013).

Membrane filter method cannot be used to differentiate between fiber types. For the knowledge of different types of fibers in the sample, different forms of microscopy have to be used. Polarized light microscopy (PLM) is the cheapest technique for obtaining information about fiber characteristics. The fibers in this method must have at least 1 μm in width. Additional information can be provided by more expensive Electron microscopy technique. Combination of Scanning electron microscopy (SEM) and energy dispersive X-ray analysis (EDXA) can normally be used to characterize fibers greater than 0.2μm in width. Analytical transmission electron microscopy (TEM) is acknowledged as the most expensive yet the most accurate method to examine crystalline inorganic fibers with width down to 0.01μm and provides information about their structure and chemical composition (Who, 1997).

3.2 Fluorescence imaging

Disadvantages connected to using radioisotopes in imaging methods can be overcome using Fluorescence imaging (FLI) (Nahar *et al.*, 2013). FLI is built on energy absorption which comes from an external excitation light. Particles are tagged with fluorescence imaging agents such as green fluorescent protein, red fluorescent protein and organic/inorganic fluorescent dyes. This method analyses a propagation of nonionizing radiation light photons. (Park *et al.*, 2012).
After the deposition in vivo, images are taken and imported into image analyzer for particle quantification. For in vivo measurement, problems with scattered, reflected and absorbed fluorescent light can occur. For in vitro measurement, fluorescent particles are usually rinsed out using prepared solution and the relative concentration of fluorescent tracers is measured by fluorometer (Zhou *et al.*, 2011). It is important to note that for testing to be relevant, fluorescent particles with linear connection between their concentration and intensity of fluorescence have to be chosen (Belka *et al.*, 2014). FLI can be a simple and economical substitute when other methods such as gravimetry or radionuclide imaging are not applicable.

4 Other methods

4.1 Magnetic resonance imaging

For a long time, Magnetic resonance imaging (MRI) has been used to image lung tissue, ventilation and to provide anatomical information for combination with data obtained from other imaging methods to create multimodal systems (Park *et al.*, 2012).

Use of MRI has a significant advantage over methods such as SPET or PET because it lacks the problems associated with radiolabeling the substances, problems with safety and necessary expertise for running the experiments. Imaging methods using radionuclides have brought more clarity into the understanding of the aerosol deposition, however, these methods are limited by the use of radiation. Therefore, the techniques which do not require use of radionuclides come to consideration. MRI is one of them (Nahar *et al.*, 2013).

Nuclear magnetic resonance (NMR) phenomena is applied in MRI. It is based on the use of nonionizable radiation, several diverse intrinsic tissue contrast mechanisms and 2D and 3D arbitrary orientations. Generation of the images is based on the signal acquired from nuclei with either full or half integer values of spin proportional to its angular momentum, which is a consequence of an odd number of protons and/or neutrons, as found in e.g.: ^{1}H, ^{3}He, ^{15}Na. MRI is mostly based on imaging of hydrogen atoms that are found in the majority of body tissues (Thompson and Finlay, 2012). For the imaging of ventilation and aerosol delivery in lungs a hyperpolarized 3He or ^{129}Xe gases are used. They can produce a higher level of polarization and therefore, are better for imaging than water protons. In order for the gases to produce an increased polarization efficiency, laser light is needed to increase the energy of the nuclei (Nahar *et al.*, 2013).

MRI can also be used for imaging of superparamagnetic iron oxide particles. In this case, a detection via direct perturbation of the static magnetic field is used and not the mechanism of T1 (longitudinal relaxation time constant) or T2 (transverse relaxation time constant) times reduction which is much more common. For the T1, T2 approach in the MRI imaging, two perpendicular magnetic fields are used: static external homogenous magnetic field ($B_{0)}$ and radiofrequency (RF) electromagnetic field (B_1). Magnetic momentum (represented by vector **M**) in the sample or region of interest is first aligned by B_0 field (Figure 9(A)), afterward B_1 is applied perpendicular to the B_0 and if a correct frequency is used, **M** is excited from its position and starts to rotate in transverse x-y plane (Figure 9(B)). Each atom has its own gyromagnetic ratio calculated for specific intensity of magnetic field and from this ratio it is possible to calculate an own frequency of atom which is necessary for the magnetic momentum to be excited. Magnetization of excited momentum can be afterward detected via RF electromagnetic field which is detected as a current by the receiver antennae (Figure 9(C)). Localization of the signals in the space is provided by magnetic field gradients. Frequency spectrum of the received signals is directly related to the distribution of chosen nuclei in the space. The same but more

complex principles than ones mentioned above are used for 3D localization (Thompson and Finlay, 2012).

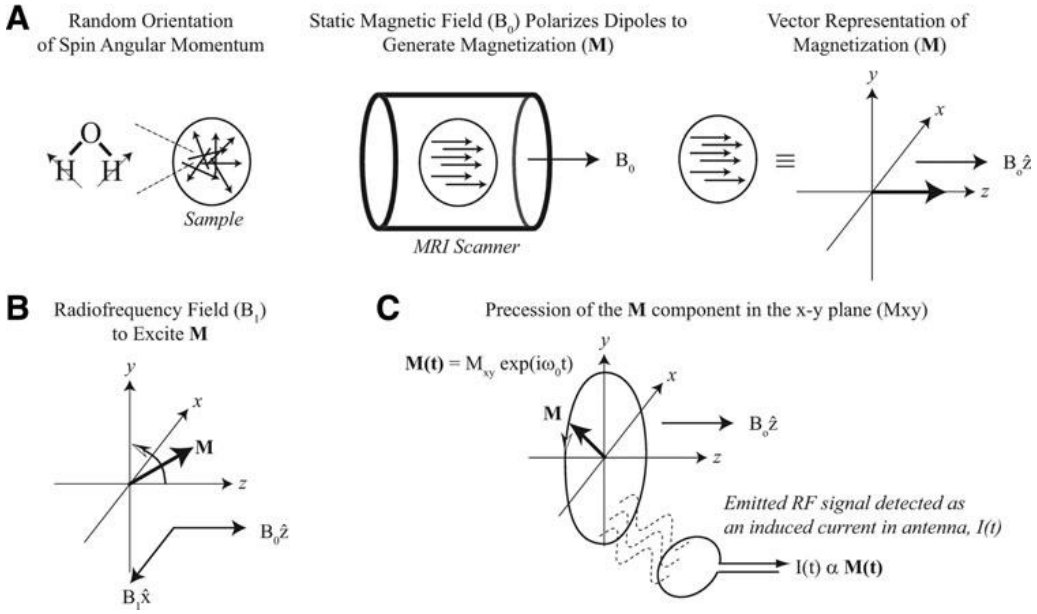

Figure 9: Illustrative simplified principle of NMR (Thompson and Finlay, 2012).

In MRI (Figure 10), the contrast agent is used as a surrogate marker for aerosol deposition. This means that just like in SPECT, MRI only provides information about the contrast agent deposition. The same incorporation of the tracer into the drug like in PET imaging would be necessary to enable the imaging of drug delivery (Thompson and Finlay, 2012).

The future of the MRI for the study the of deposition depends on progress in the contrast agent development. More work and reduction in trace levels is needed, to make it competitive to traditionally used radionuclide imaging methods (Thompson and Finlay, 2012).

Figure 10: Modern MRI scanner (Siemens, 2010).

4.2 Gravimetry

Gravimetry is one of the typical and simple methods for deposition analysis. It is a process where change in mass is used to determine the mass or concentration of the substance. In this method, model or the parts of the model are simply weighed before and after the experiment using the laboratory microscale (Grgic, Finlay and Heenan, 2004).

This method is relatively easy and affordable, in comparison with methods such as radionuclide imaging. On the other hand, deposition can only be assessed in demountable parts of the model and focal point of deposition cannot be located. All parts of the model have to fit within the used laboratory microscale (Figure 11). For the validation and possibility of repetition, a workplace in laboratory has to be protected from direct sunlight, vibrations and air current. Constant temperature needs to be guaranteed. When it is not possible to reach the requirements of ideal workplace, it is preferable to use other method to avoid the biased deposition results. (Lizal, 2012)

Figure 11: Commercial laboratory microscale (capacity of 300 g and 0.00001 g readability) (Contech India, 2008).

4.3 Sampler

Measuring or modeling the full particle size distribution in live subjects or adequate models is frequently made by using methods such as PET, SPECT, gravimetry etc. which can estimate a deposition fraction in individual segments or total deposition in these models. Samplers can evaluate the particle deposition in lung directly. Such samplers can be either used to predict total deposition or regional deposition. Total deposition samplers do not provide information about the area of deposition in respiratory system, but the data about the total aerosol dose is more accurate. In the case when information about the region of deposition is also an important factor, penetration-based samplers (regional deposition samplers (RDS)) should be used.

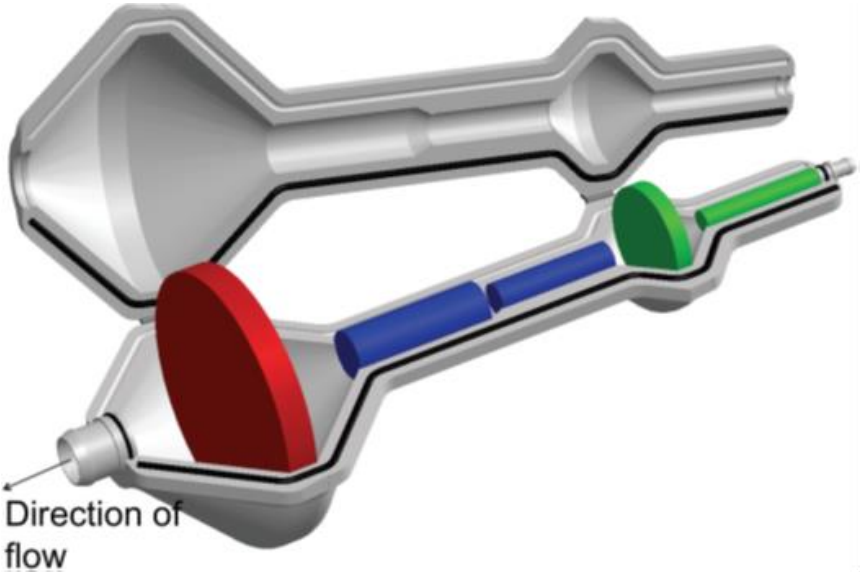

Figure 12: Computer-aided design drawing of the RDS holding two foam inserts to match the deposition in the head airways (first two green substrates), two foam inserts to match the deposition in the tracheobronchial region (next two blue substrates), and nylon mesh screens to match the deposition in the alveolar region (last red substrate).

Showed RDS (Figure 12) mimics regional particle deposition in 3 main sections of the respiratory tract: head airways, tracheobronchial and alveolar region. To match deposition in head airway and in tracheobronchial, two pieces of foam in each section were used. For the alveolar region, foam was substituted by the nylon mesh screen due to the unreasonable properties suggested for foam by deposition model. Despite the accuracy for mass-based measurement, this method is not suitable for gravimetric analysis due to the foam hygroscopicity. The nylon mesh screens also are too large to fit within most commercial microbalances.

Fluorescence analysis is used as suitable chemical examination to estimate the aerosol deposition. Foam inserts and nylon mesh screens are put into the centrifuge for extraction and followed by quantification of the fluorescently labeled particles by excitation-emission spectroscopy. Using sampler for deposition analysis is relatively simple, quick and practical. RDS provides valid data about deposition for aerosol size distribution resulting from combustion, fumes, mists, engineered nanoparticles etc. Biased data may be obtained from procedures resulting in large aerosol size distributions (e.g. grinding). In the future, a redesign of a holder should be considered to minimize the losses. Despite the simplicity of this method, one of the main disadvantages is the necessity to redesign the sampler, in order to cover different physiological or breathing conditions (Koehler and Volckens, 2013).

4.4 Simulation

The use of modelling methods for study of airflow and particle deposition can make a significant difference in understanding of the deposition and delivery of drug particles or

pollutants into the human lung. However, validation of such acquired data is necessary. Due to poor quality of the information from experimental studies the use of this method has been limited. Present improvement in 3D imaging methods provides opportunity for more experimental data and thus necessary validation of these computer deposition models. (Fleming *et al.*, 2015).

Inhalation of radioactive aerosol by human subjects always causes concerns about safety. Modelling overcomes this problem, moreover, it can provide information about local deposition patterns which can be obtained from in vivo experiment only with less accuracy. Another good reason for implementing deposition modeling is the need for understanding of particle deposition in all members of population and all age groups where experimental studies are not always permitted due to ethical considerations or not feasible for health reasons and different breathing conditions. It allows modeling of different lung volumes, particle sizes and breathing parameters while the experimental data refers only to specific human subject and defined inhalation conditions.

Current models for particle deposition can be grouped into four categories. Two categories refer to the area of interest in the lung and another two refer to the methods for predicting the rate of deposition and transport of inhaled particles.

Whole lung and local scale approach

First category is dived into **whole lung models** and **local scale models**.
In the whole lung models, deposition and transport of inhaled particles are treated independently due to extreme complexity of the airway system. Whole lung approach is solved by analytical models. Therefore, analytical equations are used for particle deposition in individual models (Hofmann, 2011). These models employ simple lung geometry and the equations for 1D transport. They provide information about total and regional lung deposition of inhaled particles.

Deposition models in **whole lung approach** can be divided into two main categories: empirical/semi-empirical and mechanistic models.

In the **empirical** and **semi-empirical models**, respiratory tract is considered as the numerous anatomical compartments in row through which aerosol passes during the breathing period (Figure 13). The efficiency of deposition in each compartment is derived from experimental data and these compartments are treated as filters. Usefulness of these models is in their simplicity and easy use.

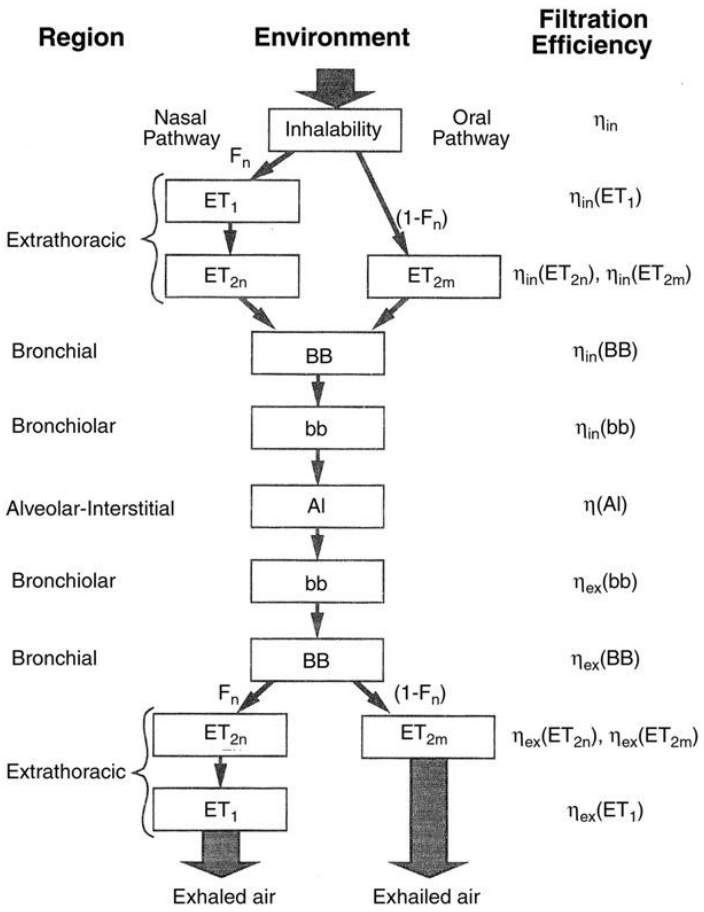

Figure 13: Example of empirical representation of inhalability and deposition of particles in human respiratory tract by passing through numerous filters (Hofmann, 2011).

Mechanistic models use more complex structure, physiology and mathematical equations therefore deposition is calculated based on more realistic structure (Rostami, 2009). There are different types of such models. Few of them are for example:

One-dimensional cross-section model

One-dimensional cross-section or ‘‘trumpet’’ model simplifies the airway system in a 1D, variable cross-section channel. Individual cross-sections are dependent on the number of the generation of a given symmetric lung model. Hence each airway branch within a given generation has identical dimensions and is characterized by its axial distance from the origin of the trachea. Drawback of this approach is its inability to simulate the asymmetry of the human airway. On the other hand, this model includes exact mathematical formulations and adding exact loss terms to the required part of respiratory tract does not cause some major problems.

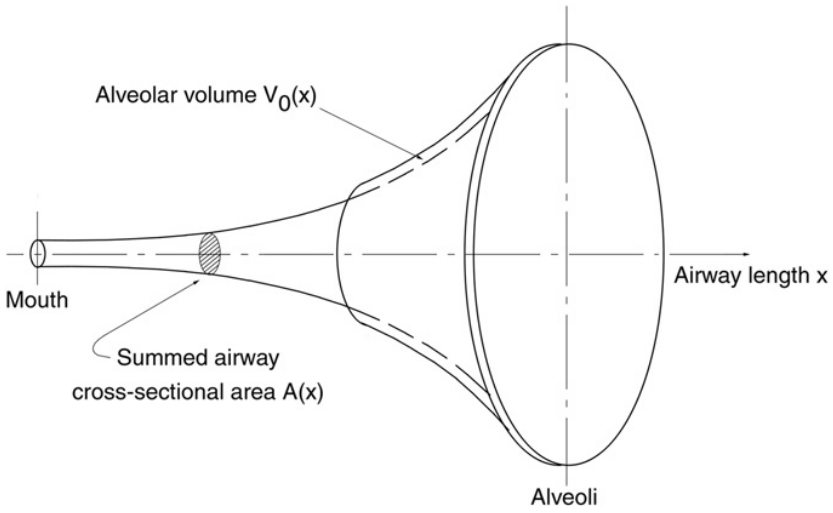

Figure 14: One dimensional cross-section or "trumpet" model (Hofmann, 2011).

Deterministic symmetric generation model

In this type of models, each airway generation consists of airways with identical dimensions and parent airways branch divided into two identical daughter airways. Due to symmetricity, deposition fraction is the same for each airway in given airway generation. Their significant advantage is the simplicity and short computational times which is the reason for frequent use of these models. On the other hand, the prediction of realistic deposition patterns in different lung structures which are not symmetric is not possible.

Deterministic asymmetric generation models

These models provide more relevant information about the particle deposition than deterministic symmetric generation models because they are based on real measurement of single airways and branches, not only on the average values. Though, complete deterministic asymmetric description of the lung is not yet available. Asymmetric models provide another few advantages over often used symmetric models e.g. mass balance equations can be solved for asymmetric lung structure, more realistic morphology provides better determination of average deposition fraction, intra- and inter-subject variations in the lungs can be determined thanks to the asymmetry. The main limitation is the lack of morphometric data for the whole lung what requires supplementation of measured airway morphometry by structurally different deterministic multiple-path models.

Stochastic asymmetric generation models

For keeping stochastic deposition models up to date, regular revision is made after release of new data or mechanism of deposition and clearance. Current models are based on the statistical analyses of the acquired morphometric data of the bronchial and acinar airways. Total regional and generational deposition in these models is calculated based on a simulation of random paths of tens or hundreds of thousands of particles. Since the information about behavior of particles within bifurcations is still limited at present to only a few bifurcation models, deposition in individual airways is based on the average behavior of an ensemble of particles as given by analytical equations. To reduce calculation times and costs, deposition of particles is substituted

by decreasing its statistical weight instead of starting the process from the entrance into the lungs.

Stochastic deposition models use the most realistic structure of human airway system, therefore allowing deposition fractions for intra- and inter-subject variability to be quantified. However, it is important to note that that stochastic geometry was obtained from single lung measurement and may not provide representative information for all subjects, although this is problem of all presently used morphometric lung models. (Hofmann, 2011)

In the **local scale approach**, numerical CFD (Computational Fluid and Particle Dynamics) methods can be used for solving deposition and transport in selected parts of human respiratory tract (Hofmann, 2011). CFD models implement a detailed 3D fluid flow and particle transport equations in contrary to simplified transport theory and help of previous experimental data used for whole-lung models. Thanks to separation of lungs into small elements, detailed information about local deposition can be acquired by this method (Rostami, 2009).

Lagrangian and Eulerian approaches

Second category comprises Lagrangian and Eulerian approaches. It is possible to find all combinations of Lagrangian, Eulerian, whole lung and local scale approach in the literature (Hofmann, 2011).

In the **Eulerian approach**, particles are not tracked individually but as a mass of particles. This population of particles is tracked through the airway and deposition in an investigated airway generation is calculated as the difference between the number (mass, or concentration) of the incoming or outgoing particles (Hofmann, 2011). It is preferable to use this approach mostly for ultrafine particles where inertia is unimportant otherwise the modifications to the approach are necessary. The Eulerian method is also common for the high concentrations and small mean diameter of particles (Rostami, 2009).

In the **Lagrangian approach**, single (representative) particles are tracked. For example, to simulating particle trajectory in airway bifurcation a few tens of thousands of simulations have to be done, in order to calculate average deposition fractions, efficiencies and deposition patterns (Hofmann, 2011). Not taking into account Brownian motion (significant mostly for ultrafine particles) into the equations automatically makes this method more suitable for larger particles (greater than 0.3 μm). Just like in Eulerian approach the corrections may be applied to adapt this method to other required parameters (Rostami, 2009).

Mostly used in Lagrangian approach, there are different techniques for solving the turbulent flow equations in these silico models e.g. DNS (direct numerical simulation), LES (large Eddy simulation) or RANS (Reynolds averaged Navier–Stokes) equations (e.g. the k–Ɛ or k–ω turbulence model equations). DNS is the most precise method that can be used for turbulent flow simulations, nevertheless, it requires long computational times and sufficient hardware equipment. LES discards the smallest scales of motion and therefore it feasible for calculations

at higher Reynolds number that DNS although the loss of small scale structures may affect the calculation of very small particles in Lagrangian approach. RANS is preferably used in CFD simulations due to its simplicity and significant reduction of computational cost. This method is not as robust as the previously mentioned ones and does not provide such detailed information, hence is suitable for a complex geometry e.g. mouth-throat, to decrease the expenses and time necessary for the calculations (Matida *et al.*, 2004).

With the technology moving forward every day, even very costly methods such as DNS and LES are getting more affordable, allowing in silico models, based on computational Fluid Dynamics (CFD) to provide scientists with more detailed information, in the experiments with various designs and conditions (Koullapis *et al.*, 2016).

5 Experimental setup

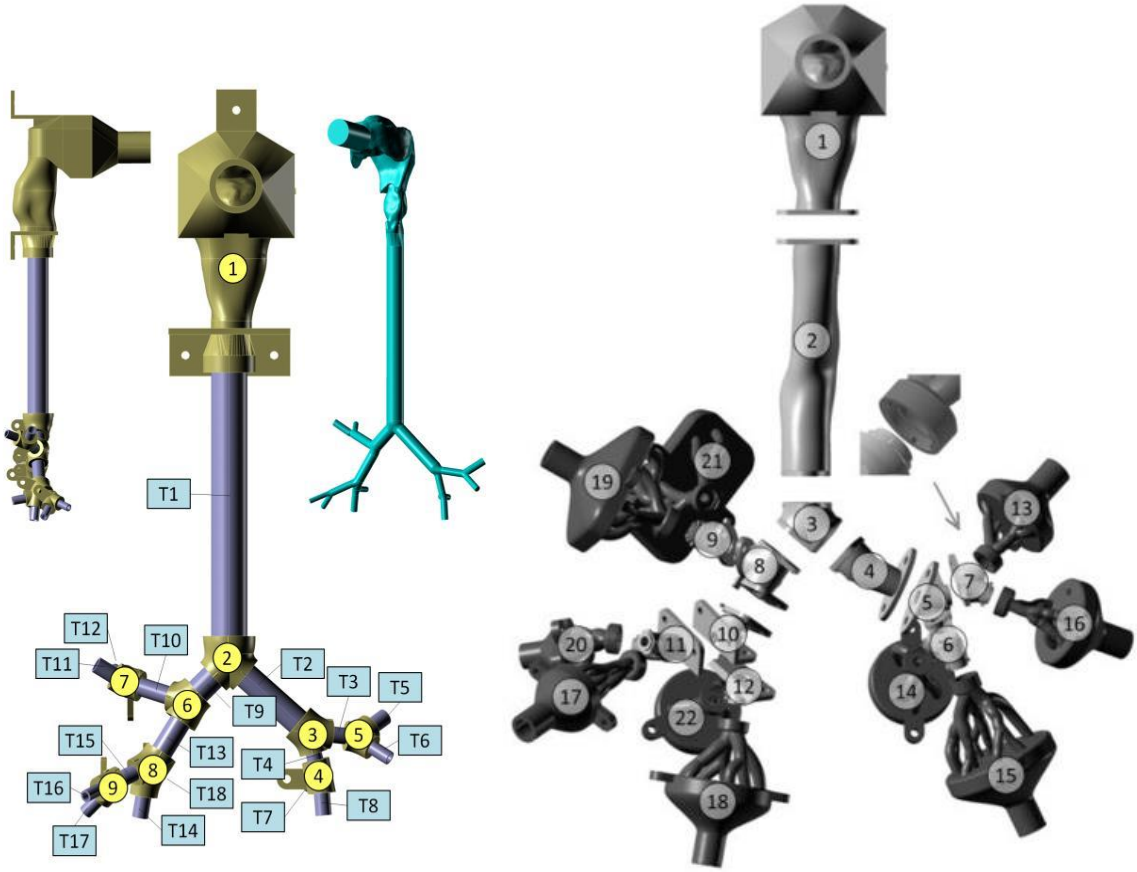

Figure 15: Segment and tube number organization of idealized lung model (left)(Lizal, 2012) and Realistic lung model (right) (Lizal et al., 2012).

Experiments analyzed in this work were performed for two flow rates and two types of model geometry (Figure 15). Two realistic and one idealized model were used for measurement of 15L/min flow rate with steady-state inhalation mode. One realistic and one idealized model were subjected to 60L/min flow rate with steady-state inhalation mode. All experiments were performed with liquid monodisperse particles of 1μm mass median aerodynamic diameter.

The first step of the preparation was to assemble a model of the respiratory tract. The manufacture and properties of the model have been described by Lizal *et al.* (2012) and Lizal (2012). The model consists of the oral cavity and the following seven generations of tree branching (TB). Model also has 10 terminal endings (see Figure 15). Model can be divided into sections to enable the measurement of aerosol deposition by methods such as optical microscopy, gravimetry, fluorescence imaging etc. Realistic lung model was fabricated by stereolithography using Somos_WaterShed XC 11122 material.

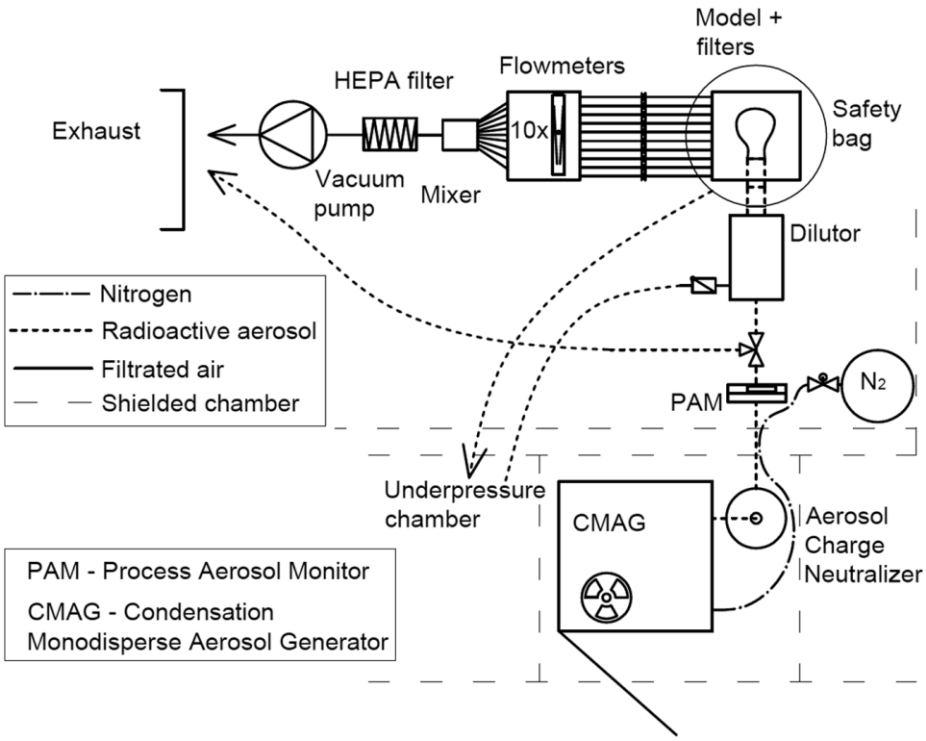

Figure 16: Layout of the experimental setup (Lizal et al., 2012).

Layout of experimental scheme is shown in (Figure 16). For the measurements, aerosol particles were generated by a TSI 3475 Condensation Monodisperse Aerosol Generator(CMAG). PET measurement which was used for analysis of the particle deposition requires radioactive aerosol. Fluorine 18 was chosen as the positron emitter due to its appropriate half-life (109 min). The modified CMAG was used to minimize the ionizing radiation in the laboratory. The produced aerosol was fed through an 85Kr-based NEKR-10 charge equilibrator and afterward into a PAM aerosol monitor for continuous particle size and concentration measurement. Glass fiber Millipore AP40 filters were attached to the output branches of the model. The whole system was sealed in a plastic bag kept in a vacuum to prevent the leakage into the laboratory. All the terminal branches with flow meters for flow rate control were united into one branch with a protective high efficiency particulate air (HEPA) filter. Configuration of the flow rates through individual branches is shown in Table 1. Detailed information about the flow rate arrangement can be found in Lizal (2012).

Branch number	13	14	15	16	17	18	19	20	21	22	Total flow rate (L/min)
Flow rate (L/min)	2.70	3.30	8.00	3.90	7.10	9.30	7.60	6.20	6.10	5.90	60
Flow rate (L/min)	1.40	1.70	4.00	2.00	3.60	4.70	3.80	3.10	3.10	3.00	30
Flow rate (L/min)	0.70	0.80	2.00	1.00	1.80	2.30	1.90	1.60	1.50	1.50	15

Table 1: Configuration of flow rates through the branches of the models used for the experiments (number of the branch corresponds to Figure 15)(Lizal, 2012).

The whole experiment took place in a protected laboratory with an underpressure ventilating system, to prevent the escape of aerosol in case of a primary safety system failure. The exposition time of the models was 10-15 min depending on radioactivity decrease caused by decay of radionuclide. After the radioactive exposure, the model was transported to a PET-CT scanner. The transportation took approximately 3 min. CT images were made first, quickly followed by PET images acquirement. The CT images were required to make a precise localization of the edges of the sections, while the PET images contain the key information about aerosol deposition (Lizal *et al.*, 2012).

6 Methodology

6.1 Work in CARIMAS

Experimental data for the analysis was acquired by CT and PET scanning, described in the previous part. CT scans containing information about the anatomy of the human lungs model and PET scans containing information about the radionuclide deposition were uploaded into the software CARIMAS 2 for further investigation.

Data loaded first into the software are automatically set as a main image. Data loaded afterward are set as a background image. For the initial preparation of the model for the analysis having CT scans set for main image is preferable due to better orientation in the scans which is necessary for correct modeling of volumes of interest (VOIs).

For a better contrast ratio, sharpness and image clearness, it is possible to adjust parameters affecting plotting of the loaded scans. For my work, best visual images were achieved when setting the rendering method to MIP (Maximum Intensity Projection) which always displays the greatest value along the view ray path. Color of the scans was set to gray which makes a good contrast with black background. Contrast slider was set to highest possible value. From different cut methods SubCube cut method acquitted well. It shows a cube around the selected area (focal Point). While zooming towards a location of interest all extra voxels around this location are cut away thus providing a better insight. Other attributes were left unchanged at default values.

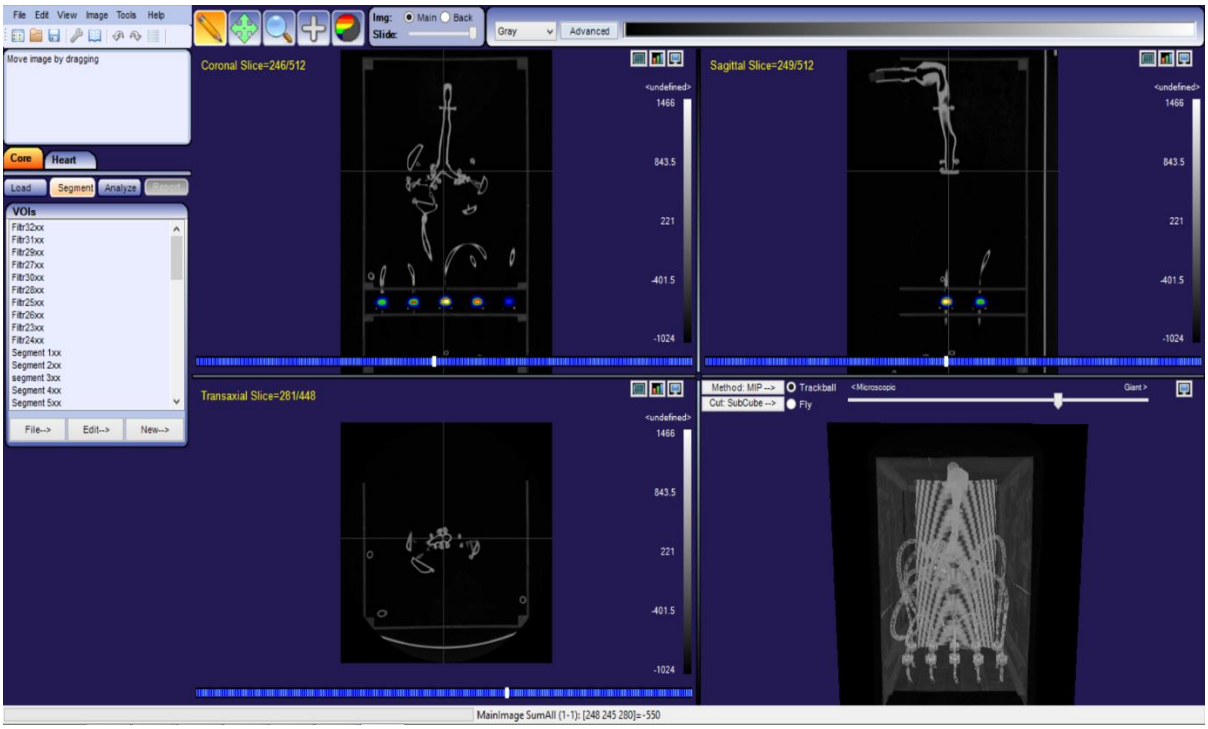

Figure 17: Workspace in CARIMAS 2. Coronal and Sagittal slice window, in top part respectively. Transaxial and 3D model window, in bottom part respectively.

For the deposition to be analyzed, the model had to be divided into VOIs, in which the amount of deposited radioactive aerosol can be detected. For the VOI it is possible to choose from prerecorded shapes such as cube, cylinder, sphere, half sphere, hollow sphere, tube, plate or 2D region of interest (ROI) which masked together with other 2D ROIs forms 3D VOI.
Shape of the VOI should be chosen to match the area that should be covered the best and to minimize additional reshaping. After selecting a suitable VOI shape, the next task is to create the VOI in the most appropriate cross sections. By the different editing modes whose icons are located on the upper left panel showed as cartoon pictures it is possible to do so. There are four different windows in a workspace (Figure 17). The one in the right bottom corner displays the model in 3D and is used just for better orientation in the space. For editing and planar insight, there are 3 different windows to choose from which display: Coronal, Sagittal and Trans axial slice. In the chosen window, we can scroll the mouse wheel or reposition the slider in the bottom part of each section to move between the acquired slices. The number behind the slash in the upper left corner in each of these three sections indicates the overall number of slices and number in front of the slash indicates the current slice. It is useful to choose the slice in which the desired area for analysis is clearly visible. If the general mode is chosen (first icon), we can simply click on the investigated place in the selected window and the other two windows will start showing the slices with corresponding position. Now that model is set in the correct axis plane, a new VOI can be created.

Before reshaping the VOI using "vertex" mode it is first important to fit it around the desired area by moving it. This is done when the "Whole" mode is chosen in the "EditVoi" section. In this mode, it is possible to move, rotate and scale the whole VOI mesh. After this step, individual points of the mesh can be moved in "vertex" mode to best match the shape of the analyzed area. Distance from the pointer in which vertices will move is controllable by "Vertex distance slider". Vertex slider set on high values is apt to move a large part of the VOI, change orientation of curvature, prolong or bend the VOI. Bending is mostly necessary in the case of cylinder VOIs. Low values set on vertex slider, accordingly small vertex brush, are good for adjusting the ends or smaller parts of the VOIs so that the whole investigated object is covered (approximately 5 mm above the surface coverage was performed to cover all of the radiation emitted from the section) but also to avoid coverage of other close objects. After casing the whole model with the VOIs, model is prepared for analysis. The program automatically calculates the mean activity (and other values such as lowest and highest activity, volume, etc.) of covered areas and displays the obtained values. Such acquired data is ready for further calculations of deposition characteristics. When the VOIs for the model are finished, it is possible to save them and import them to another model of the same type (realistic, idealized) to minimize the differences in measured activities due to change in VOI shape and volume. This approach was also used for the analysis of data in this bachelor thesis.

6.2 Deposition characteristics

With the use of Carimas software (see previous part) mean volume activities (in Bq/mL) for the individual sections were estimated. However, it was not possible to cover all model sections

with 5 mm overreach of the VOIs, due to complicated lung geometry. Thus, corrections (one for filters and other for the rest of the model) had to be made to take uncounted radioactivity into consideration. For calculating correction factors, VOIs around all the filters and the rest of the model were made. Two corrections were needed due to large difference of activity in the filter and lung model part. Correction for the filters ($Corr_f$) and for model part ($Corr_m$) were calculated based on following equations

$$Corr_f = \frac{A_{cf}}{\sum_1^p A_j} \quad (1)$$

$$Corr_m = \frac{A_{cm}}{\sum_1^n A_i} \quad (2)$$

where A_{cf}, A_{cm} are activities in correction VOIs and A_j , A_i are activities in individual sections. Total number of filters is represented by p and total number of sections by n. Corrected activity of filters and model parts can be afterward calculated as

$$A_j^* = Corr_f\ A_j \quad (3)$$

$$A_i^* = Corr_m\ A_i \quad (4)$$

The asterisk (*) marks data which has been corrected. If the correction factors are unreasonably larger or smaller than number 1 it may indicate aerosol leak or other errors in the experiment.

Corrected activities can be used to calculate deposition characteristics. Deposition fraction (DF) is defined as a ratio of number of particles deposited in the section to total number of particles in the whole model. The number of particles is assumed to be proportional to measured activity and therefore DF can be obtained as

$$DF_i = \frac{A_i^*}{\sum_1^m A_i^*} \quad (5)$$

where m total number of all sections including hoses and filters.

Comparing deposition in segments based on DF can provide misleading information because the amount of aerosol passing through the segments is different. Therefore, deposition efficiency (DE) can be used to provide more reliable data for inter-segment comparison (Lizal *et al.*, 2012). DE is defined as ratio of the number of particles deposited in the section to the number of particles entering the section

$$DE_i = \frac{A_i^*}{\sum A_f^* + A_i^*} \quad (6)$$

where A_f is sum of corrected activities in all the sections which come after ith section (including filters).

Deposition density (DD) is a ratio of DF of the section to the inner surface area of the same section

$$DD_i = \frac{DF_i}{S_i} \quad (7)$$

where S_i (m^2) is the inner surface area of section i.

These characteristics are usually plotted vs. segment number. Though, when the significant part of deposition mechanism is predicted to be inertial impaction, DE can also be plotted as function of Stokes number

$$Stk = \frac{\rho d_p^2 U}{18\mu D} \qquad (8)$$

Where d_p (μm) is the aerodynamic particle diameter, U (m/s) is the velocity, μ (Pa s) is air viscosity and D (m) is the characteristic diameter of airway. Aerodynamic diameter is defined as diameter of a sphere with density of 1000 kg/m^3 which has the same settling velocity as the considered particle.

7 Results

As mentioned before, two realistic and one idealized model were used for measurement of 15 L/min flow rate with steady-state inhalation mode. The average value from two measurements of 15 L/min flow in realistic geometry is consequently used in graphs. One realistic and one idealized model were subjected to 60L/min flow rate with steady-state inhalation mode. Mass median aerodynamic diameter of the particles used for all the experiments was 1μm.

Realistic model of human lungs is in all following graphs marked with letter "R" and the corresponding flow rate and particle aerodynamic diameter respectively. Idealized model is referred to as "Id", flow rate and particle aerodynamic diameter respectively. Sections of the model are marked as previously shown in (Figure 15). Filters in the realistic model are marked with numbers 23 to 32 and the second digit always corresponds to the number of segment after which the filter follows (filter 2**3** follows segment 1**3**, filter 3**1** follows segment 2**1** etc.). Filters in idealized lung geometry are directly named after the tube they connect to (filterT5 connects to the tube T5 etc.). Error bars represent the maximal difference found between the two measurements for 15L/min flow rate in any segments.

Activities calculated based on the analyzed data from Carimas software were corrected by correction factors (see part 5.3 Deposition characteristics). The correction factors calculated for the filters were very close to 1 for all the experiments, because a larger area between the filters allowed the VOIs to be made appropriately. Slight differences could be seen for the model part corrections. They were mainly caused by the geometries of the models which contain many small parts grouped in relatively small area. This prevented a possibility of 5mm overreach of the VOIs. For the values of correction factors and deposition characteristics see appendix A and appendix B.

DF was calculated from the corrected activities as a first characteristic. From the graph (Figure 18), it is obvious that deposition fraction in the segments of the model increases with higher flow rate. Higher number of radioactive particles deposited in segment 1 and 2 which stand for mouth and trachea respectively, while there are only slight inter-segment differences among the remaining segments (segment 3 to 22) for one breathing regime. Largest number of particles deposited on filters. Configuration of deposition directly corresponds to amount of aerosol passing through the filter which is the same for all performed experiments, including the model with idealized geometry. Maximum of deposition is located on filters 25 and 28 and minimum on the filter 23. Although minimum for "60 L/min 1μm" is not so significant.

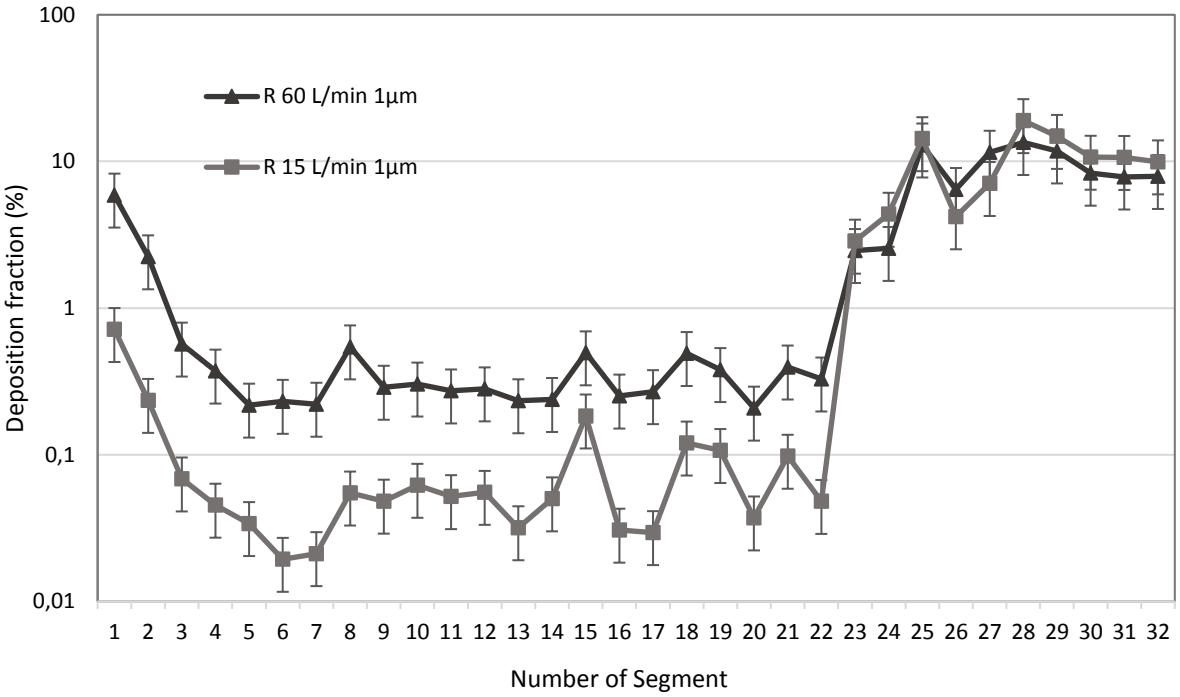

Figure 18: Deposition fraction in realistic model.

For the idealized model on the contrary to the realistic one, DF does not seem to increase with increasing flow rate (Figure 19). In the idealized model, bifurcations (Seg 2,3,6,7 and 8) are separated from branches, therefore we can observe differences of deposition in these parts. Increase of deposition fraction in bifurcations for both flow rates can be noticed. DF in filters, as stated before, corresponds to the flow through the filters. Though, it is necessary to mention that filters in graphs of idealized model geometry are in different order then filters in the realistic model geometry.

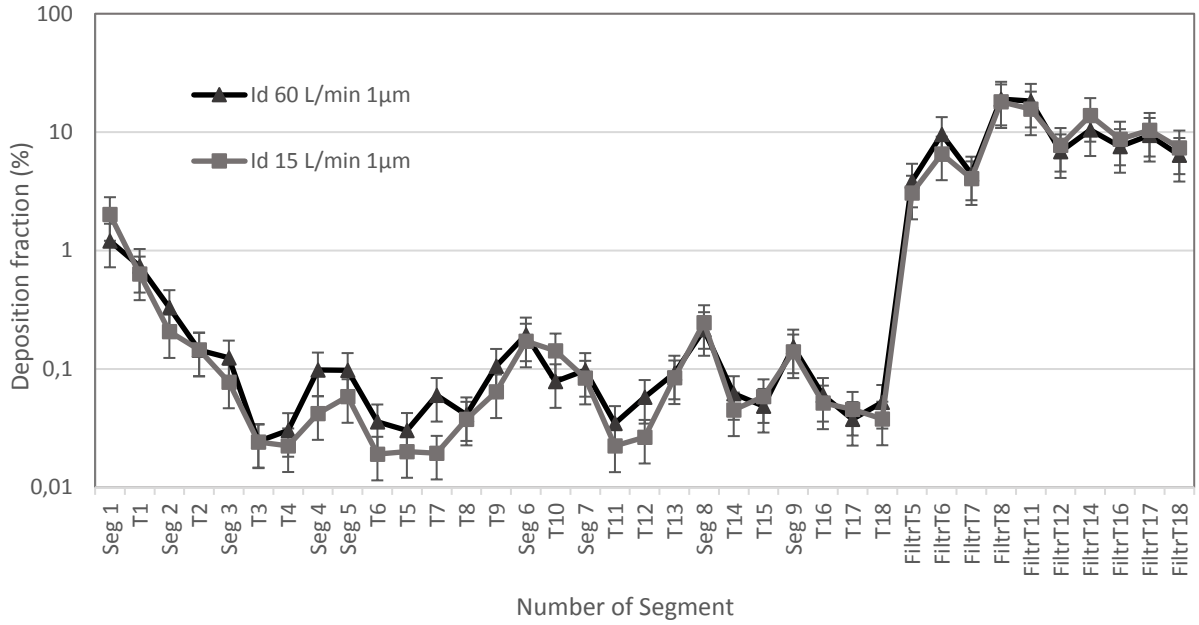

Figure 19 : Deposition fraction in idealized model.

DE was calculated next. It provides better information for comparing deposition in individual segments, because the amount of aerosol entering the segment is taken into consideration. Filters are not shown in the graph because based on the definition (see part 5.3 Deposition characteristics) they give 100% efficiency. Highest efficiencies can be observed for the mouth and trachea (segment 1 and 2) and for the second part of segments starting with segment 13 (Figure 20). Increase in segments 13 to 22 is caused by 2 or 3 bifurcations which they consist of, thus more particles deposited in these segments. Other inter-segment differences are very small.

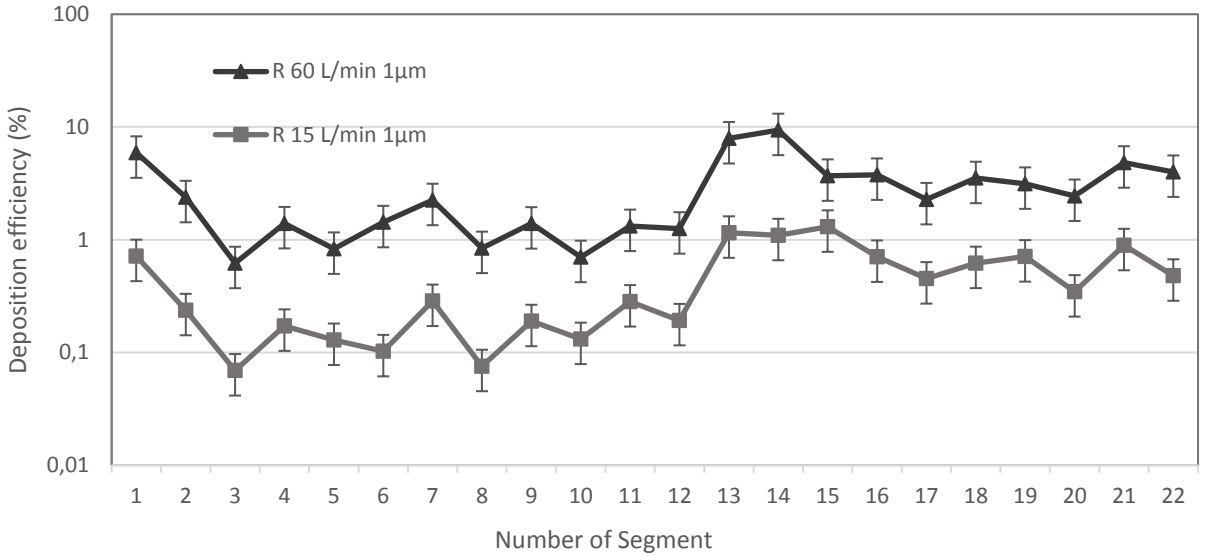

Figure 20 : Deposition efficiency in realistic model.

As indicated before in DF graph (Figure 19) also DE in the model with idealized geometry shows no notable difference for higher flow rate (Figure 21). Peaks of DE are located in T3, Seg 5, T6 and T5 and their DE even highly overcomes DE in mouth and trachea (Seg1, T1).

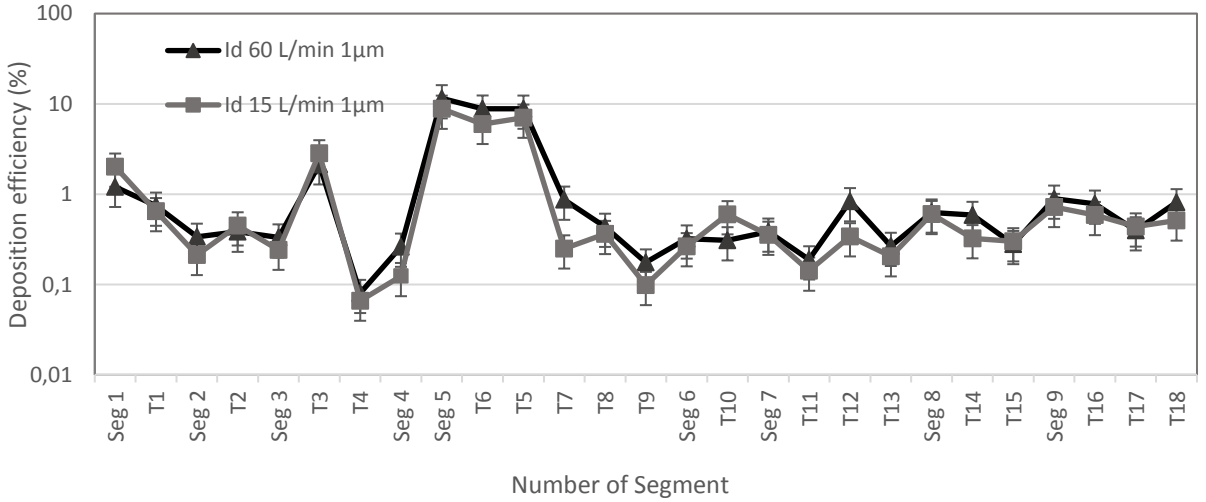

Figure 21: Deposition efficiency in idealized model.

DD is another often calculated characteristic. It is a ratio of deposited particles in the segment to its surface area. Hence, it is useful characteristic for toxicology and pharmacology, because

it tells how much aerosol the tissue absorbs, in that specific section (Lizal, 2012). DD for the realistic model is lower for the segments 13 to 22 (Figure 22) which previously had higher DE. Lower values are caused by relatively large surface area of these segments.

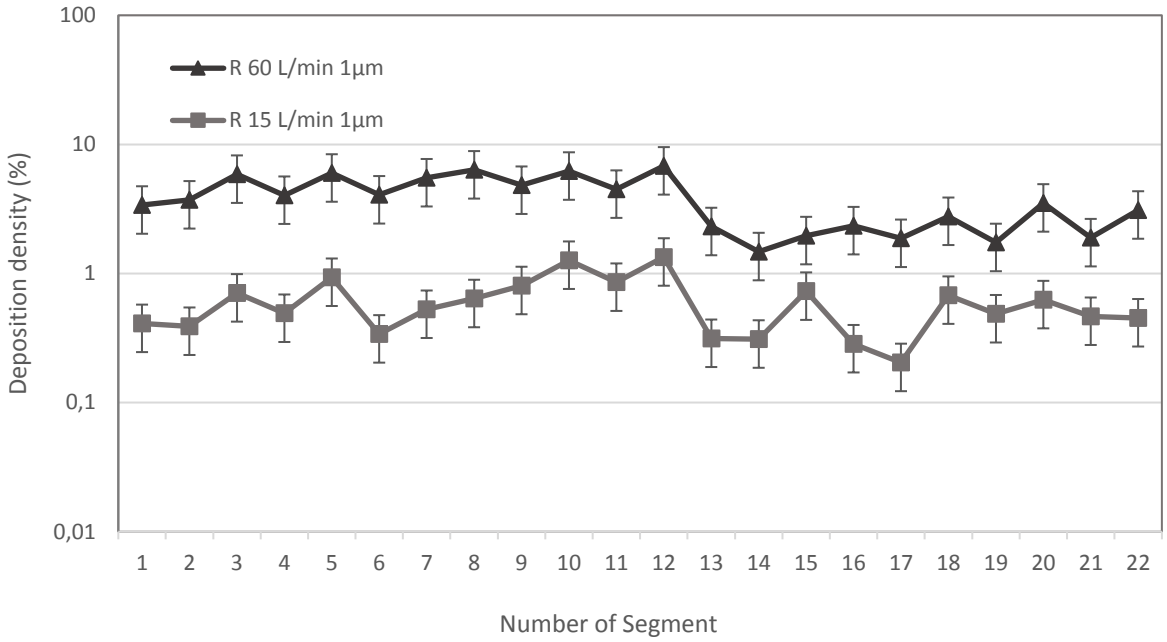

Figure 22: Deposition density in realistic model.

DD for idealized model, just like the previous characteristics shows no difference for change in the flow rate (Figure 23). Peaks of DD are located in segments of the model (Seg 2 to Seg 9), which also had the higher deposition fraction.

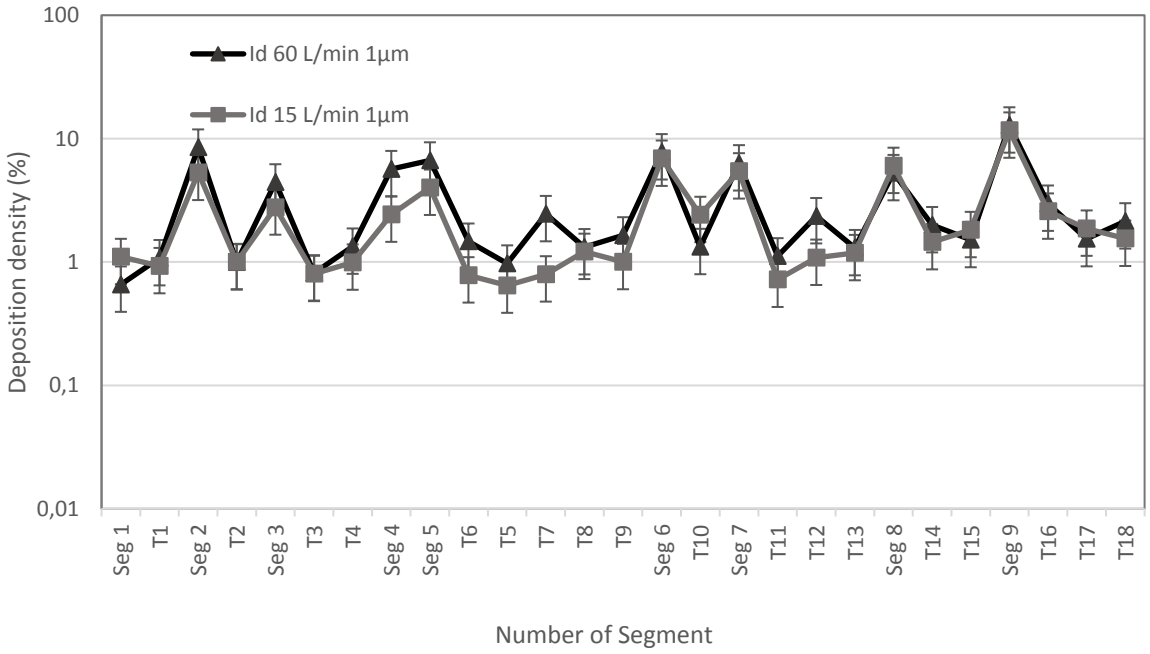

Figure 23: Deposition density in idealized model.

Comparison with other studies

DE was compared to the previously published particle deposition measurements (Figure 24) made by Zhou and Cheng (2005).

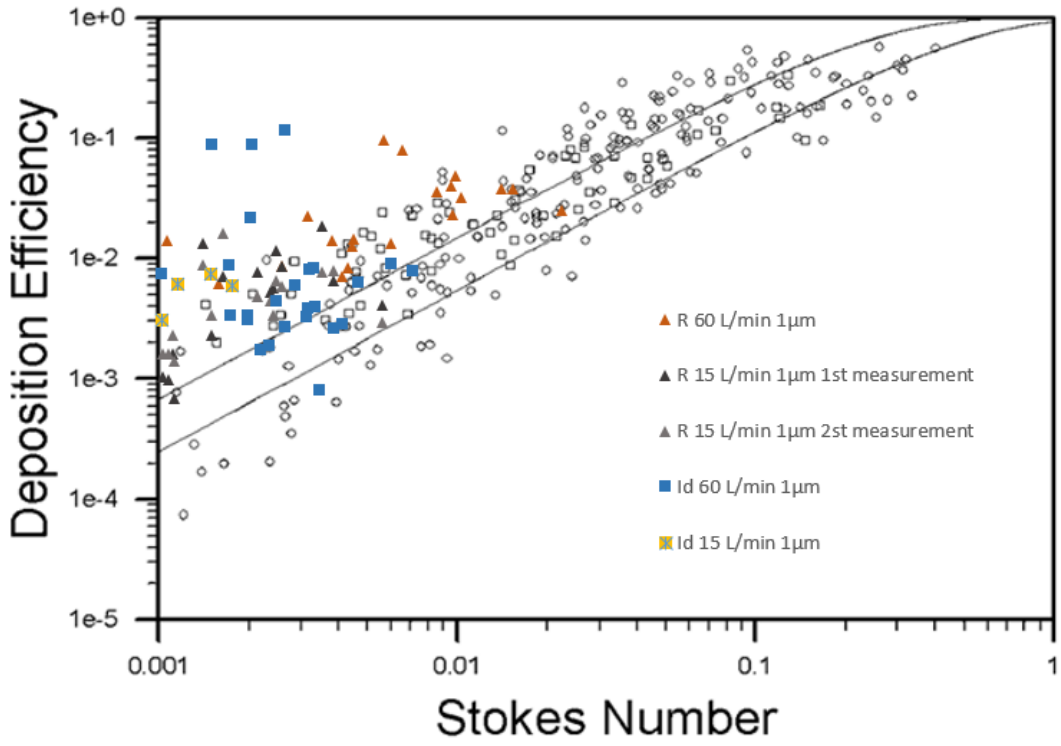

Figure 24: Comparison with previous studies. Empty marks and lines refer to the previously acquired data. Modified from (Zhou and Cheng, 2005).

Stokes number (horizontal axis of the graph) is known to describe the probability of particle deposition via impaction (Carvalho *et al.*, 2011). For good comparing option, the same method for choosing characteristic diameter in calculations of Stokes number was used. DE for the realistic geometry is increasing with increasing Stokes number which suggest that inertial impaction was predominant deposition mechanism. This data also shows good agreement with previous studies. For the idealized geometry, DE does not necessarily increase with increasing Stokes number, therefore other deposition mechanisms may be expected to play a significant role along with inertial impaction in particle deposition for some regions of the model. Three points (blue square marks) which stand out in the graph (Figure 24), are Seg5, T5 and T6 for "Id 60 L/min 1 µm" experiment. They represent peaks of DE in the idealized model, as seen in Figure 21.

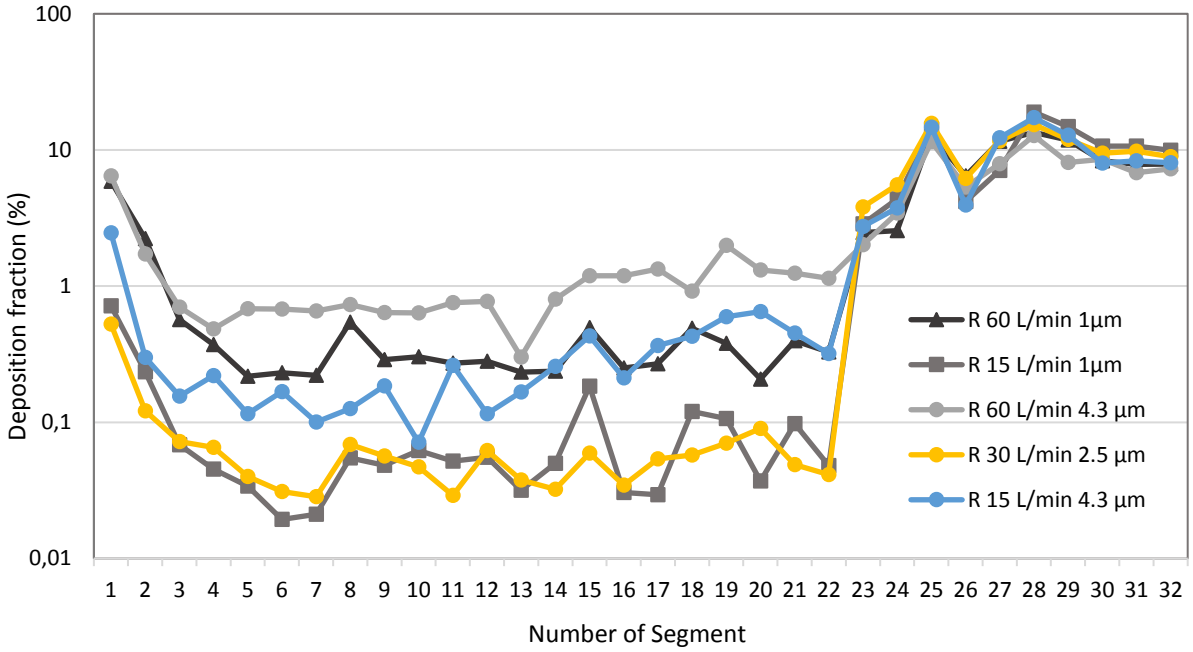

Figure 25: Comparison of deposition fraction with previous studies for realistic model geometry. Grey, yellow and blue line with circular marks refer to previous studies. Error bars are not displayed to ensure good readability. Modified from (Lizal, 2012).

DF was plotted into the graph (Figure 25) with data previously published in (Lizal, 2012). For flowrate 15 L/min and 1 µm particles, its DF even exceeds DF for higher flowrate of 30 L/min and bigger particles with 2.5 µm aerodynamic diameter which is worth meditation. Largest differences in DF can be seen in lower segments (segment 14,15,18,19,21) because smaller particles tend to deposit more in lower parts of respiratory tract and additional deposition mechanisms get involved in small segment and for low flowrates. The fact that DF for 60 L/min and 1 µm particles shows similar or lower DF in lower respiratory tract than experiment "R 15 L/min 4.3 µm" is interesting as well. Important reason may be the exponential growth of DF with increasing particle size (in our case particle size increased from 1 µm to 4.3 µm) and lower flowrate so that more particles reach the bottom part of lung due to better ability to follow the streamline. Relatively low airflow (15 L/min) and small branches may then increase the possibility of deposition of these particles by sedimentation.

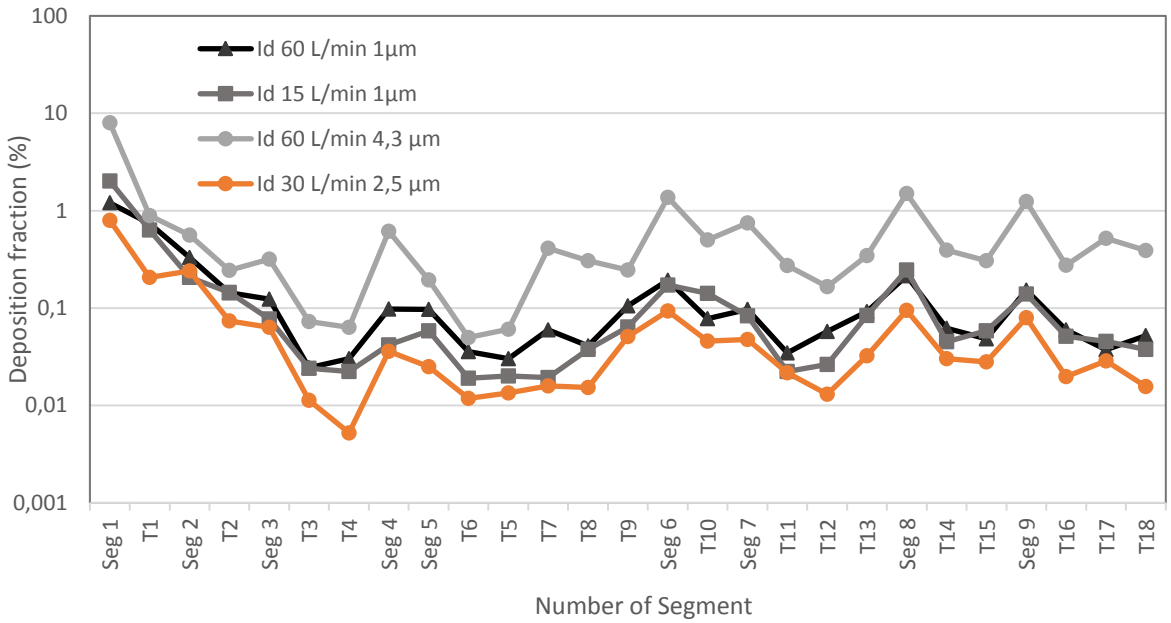

Figure 26: Comparison of deposition fraction with previous studies for idealized geometry. Error bars are not displayed to ensure good readability. Light grey and orange lines with circular marks represent data from previous studies. Modified from (Lizal, 2012).

Very similar values of DF can be seen for the experiments "Id 60 L/min 1 µm", "Id 15 L/min 1 µm", "Id 30 L/min 2.5 µm". DF of "Id 30 L/min 2.5 µm" experiment show slightly lower values than previously mentioned measurements. DF for filters is not shown due to better possibility of segment comparison in the graph and it shows no notable difference between the measurements. DF of filters in idealized model can be seen in Figure 19.

7.1 Stability of analysis

All the data presented in this bachelor thesis was obtained using Carimas software. Therefore, either for the accuracy of this or future studies it is important to make sure that the analyses in the software provide reliable data. As mentioned in previous chapters, corrections had to be applied on the acquired activities. The reason for the corrections was inability to cover all segments with overreach due to very small distance between some parts of the model. This problem was even worse for the model with idealized geometry, which consists of more parts in a small area. Many VOIs had to be made close to each other, while it is necessary to avoid accounting some activity twice. Additional factors affecting corrections and overall accuracy of the output, when talking about software is for example the size of the voxel in the Carimas software and inability to display borders of the VOIs for two and more VOIs selected at once, which makes positioning the VOI to its correct place even more difficult. Few precautions were made to provide reliable data. To avoid some systematical error and to confirm the stability of Carimas software all CT and PET scan were made twice. The first scan was made as soon as possible after exposing the model to the radioactive aerosol and the results from this measurement are presented in this work. Second scan was made with some time delay, which

caused significant decrease of activity but should not affect deposition characteristics, when analyzed correctly. The results of the scans can be seen in Figure 27 and Figure 28.

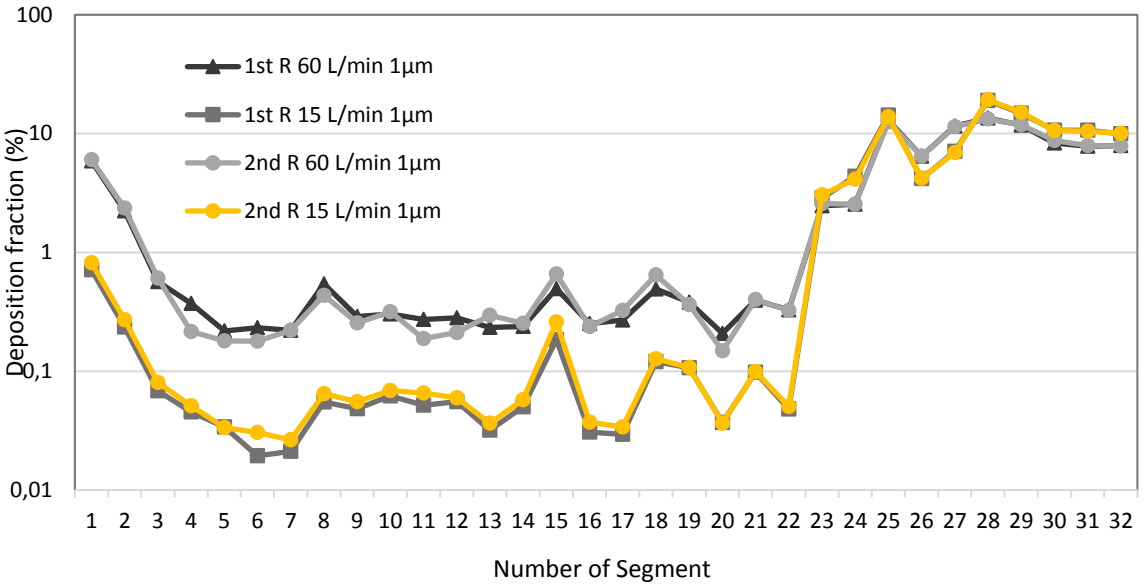

Figure 27: Comparison of DF in first and second scans made for realistic model geometry.

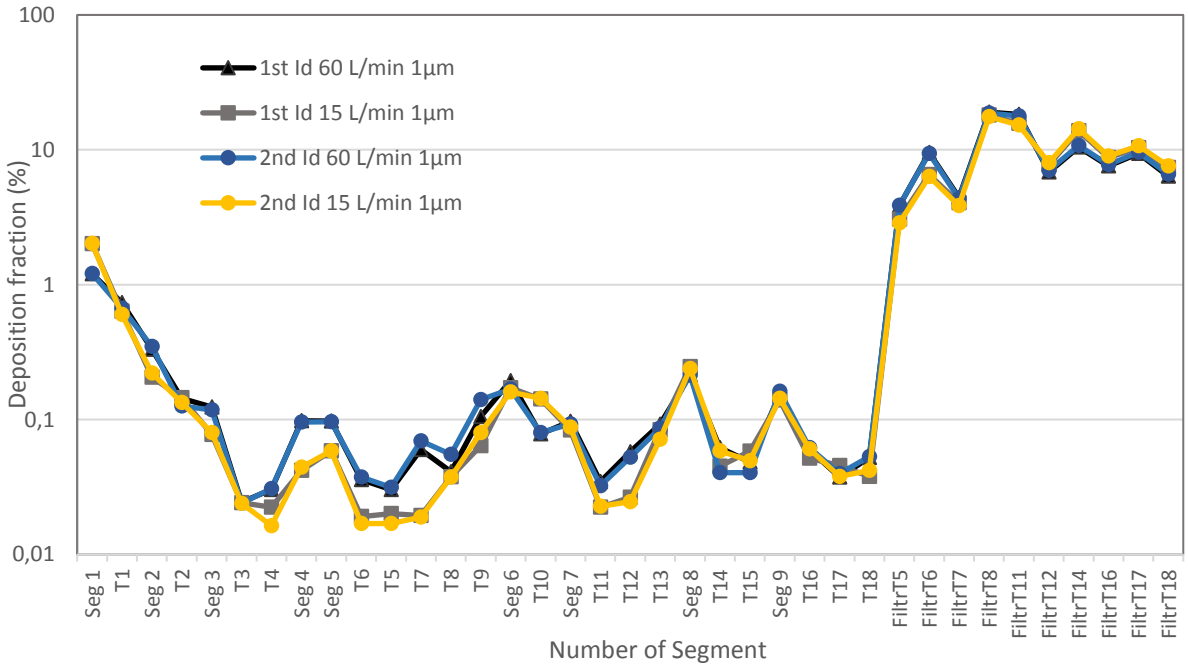

Figure 28: Comparison of DF in first and second scans made for idealized model geometry.

First and second scans show a very good agreement and confirm the stability of repeated analyses. To prevent errors made by person processing the scans, all experiments have been analyzed by another trained person. Presented data and correction factors for all measurements showed a good agreement. For the comparison of correction factors in the main and control analyses see Appendix C.

8 Discussion

In the realistic geometry models, all calculated deposition characteristics increased significantly with increasing flow rate. In general, higher flow rate results in higher DE. This assertion was true in our case. Confirmed by the increasing DE with increasing Stokes number, inertial impaction can be referred to as a main deposition mechanism.

More noteworthy results were obtained for the idealized geometry. Increase of flow rate from 15 to 60 L/min caused only slight increase of deposition characteristics, mostly in the upper and middle parts of airways. DF in lower parts of respiratory tract (segment 6 to 9 and T13 to T18) (Figure 19), was similar or even higher in some segments for 15 L/min flowrate. DE was highest for the parts with lowest flow rate (T3, Seg 5, T6 and T5) (Figure 21). It means that higher velocity of aerosol does not cause more particles to deposit in the model. This statement is confirmed by the fact that DE does not increase with rising Stokes number, therefore inertial impaction is not the main deposition mechanism. Very slight increase of deposition characteristics may be explained by low Stokes numbers (lower than 0.001 in majority of segments), which mean that particles follow the streamline and do not deposit. Low rise of deposition, in comparison with realistic model, is also caused by glass tubes used for the idealized model. These glass tubes have almost no surface roughness, straight axis and diameter within one tube is constant, therefore, for the very same region (the same particle size and flowrate), realistic model has slightly higher Stokes number. Slight increase of the deposition in the small parts of the airway (lower respiratory tract) and for lower flowrate (15 L/min) indicates effect of sedimentation. This minor increase is visible also in the model with realistic geometry. Overall low deposition in the model is also a consequence of particle diameter. DF is lowest for particles with diameters from 0.1 to 1 μm due to decreasing mass, thus descending influence of sedimentation and yet low influence of diffusion, due to relatively large diameter(Asgharian *et al.*, 2006).

What should be raising the awareness is the low DF of the experiment with 30 L/min airflow and 2.5 μm particles, compared to current study. For realistic model geometry, experiment "R 30 L/min 2.5 μm" shows very similar DF to "R 15 L/min 1 μm" (Figure 25). For the same flow rate and particle size, DF in idealized geometry for "Id 15 L/min 1 μm" experiment is even higher than DF of "Id 30 L/min 2.5 μm" (Figure 26). This resemblance in deposition may be partly explained (as mentioned in the previous paragraph) by low Stokes numbers (in this case lower than 0.01) which mean that particles follow the streamline. Since this fact explains the similarities just partially, at this point in time, it is not possible to clearly say what exactly caused such results and it is certainly necessary to repeat these measurements more times to provide a valid statement. Few of the measurements were already performed, however, the data has not been processed yet. Another one of the possibilities, of such low deposition characteristics, may be an error in evaluation of particle aerodynamic diameter.

9 Conclusions

In the presented study, analyses of deposition of inhaled particles in the model of human lung were performed. Two types of model geometry and two types of airflow were applied, particle diameter remained the same. Resulting deposition characteristics were calculated from volumetric radioactivity and data was analyzed.

The main outcomes of this thesis include the detailed information about the deposition fraction, efficiency and density in studied geometries and the process of obtaining these values. We can state that the change in the flowrate has very insignificant influence on deposition in the idealized geometry compared to the realistic one. It is obvious that all results obtained for idealized model are very significantly affected by the simplified geometry (especially the smooth walls and constant diameter of tubes). In the comparison with data from previous studies, surprising values of the deposition fraction could be observed for both geometries. It is necessary to continue in further investigation to present conclusions. Effect of inertial impaction was lower compared to previous experiments as the 1 μm particles managed to follow the streamlines due to the low Stokes numbers. This effect was more pronounced in the idealized model, due to the simplifications of the geometry. Additional rise of activity in small airways and for low flowrates, in both geometries, is an effect of sedimentation, which becomes important mostly in such conditions. For the realistic geometry, predominant deposition mechanism was inertial impaction.

Good stability of the analysis, in the used software, was confirmed by repetition of scanning procedures, after some time delay, and repeated analyses of these scans as well as performing the same analyses independently by another trained person. Therefore, it is safe to say that for the carefully performed experiments and analyses made by a trained person, good reliability of results can be reached by use of this software.

Further attention should be paid to aerosol behavior in the respiratory tract in the future. Experiments with different particle sizes, flowrates and breathing regimes should be performed, to provide enough information applicable for the comparison with previous studies and for the therapeutic, safety or scientific purposes.

Bibliography

ASGHARIAN, B., O. T. PRICE AND W. HOFMANN Prediction of particle deposition in the human lung using realistic models of lung ventilation. Journal of Aerosol Science, Oct 2006, 37(10), 1209-1221.

BELKA, M., J. LIPPAY, F. LIZAL, J. JEDELSKY, et al. Comparison of methods for evaluation of aerosol deposition in the model of human lungs. In T. VIT, P. DANCOVA AND P. NOVOTNY eds. *Efm13 - Experimental Fluid Mechanics 2013.* Cedex A: E D P Sciences, 2014, vol. 67.

BERRIDGE, M. S., D. L. HEALD AND Z. LEE Imaging studies of biodistribution and kinetics in drug development. Drug Development Research, Jun 2003, 59(2), 208-226.

CARVALHO, T. C., J. I. PETERS AND R. O. WILLIAMS Influence of particle size on regional lung deposition What evidence is there? International Journal of Pharmaceutics, Mar 2011, 406(1-2), 1-10.

CHENG, Y. S. Mechanisms of Pharmaceutical Aerosol Deposition in the Respiratory Tract. Aaps Pharmscitech, Jun 2014, 15(3), 630-640.

CONTECH INDIA. Analytical Balances. 2008. Avaialble at: < http://www.contechindia.com/images/analytical-indirect-loading-balances-full-image.jpg >. Accessed on: 02.02.2017.

CONWAY, J. Lung imaging - Two dimensional gamma scintigraphy, SPECT, CT and PET. Advanced Drug Delivery Reviews, Mar 2012, 64(4), 357-368.

ERGO. Smal-field gamma camera. 2011. Avaialble at: < http://www.medicalexpo.com/prod/digirad/product-81316-613741.html >. Accessed on: 20.02.2017.

FLEMING, J., J. CONWAY, C. MAJORAL, I. KATZ, et al. Controlled, Parametric, Individualized, 2-D and 3-D Imaging Measurements of Aerosol Deposition in the Respiratory Tract of Asthmatic Human Subjects for Model Validation. Journal of Aerosol Medicine and Pulmonary Drug Delivery, Dec 2015, 28(6), 432-451.

FLEMING, J., J. CONWAY, C. MAJORAL, L. TOSSICI-BOLT, et al. The Use of Combined Single Photon Emission Computed Tomography and X-ray Computed Tomography to Assess the Fate of Inhaled Aerosol. Journal of Aerosol Medicine and Pulmonary Drug Delivery, Feb 2011, 24(1), 49-60.

FRONTIERS. Annihilation reaction and the subsequent coincidence detection. 2013. Avaialble at: < http://www.frontiersin.org/files/Articles/57309/fonc-03-00208-HTML/image_m/fonc-03-00208-g001.jpg >. Accessed on: 20.02.2017.

GE HEALTHCARE. SPECT-CT. 2004. Avaialble at: < http://perform.concordia.ca/corebooking/specs.asp?asset=39 >. Accessed on: 20.2.2017.

GRGIC, B., W. H. FINLAY, P. K. P. BURNELL AND A. F. HEENAN In vitro intersubject and intrasubject deposition measurements in realistic mouth-throat geometries. Journal of Aerosol Science, Aug 2004a, 35(8), 1025-1040.

GRGIC, B., W. H. FINLAY AND A. F. HEENAN Regional aerosol deposition and flow measurements in an idealized mouth and throat. Journal of Aerosol Science, Jan 2004b, 35(1), 21-32.

HOFMANN, W. Modelling inhaled particle deposition in the human lung-A review. Journal of Aerosol Science, Oct 2011, 42(10), 693-724.

HOLLY, T. A., B. G. ABBOTT, M. AL-MALLAH, D. A. CALNON, et al. Single photon-emission computed tomography. Journal of Nuclear Cardiology, Oct 2010, 17(5), 941-973.

KOEHLER, K. A. AND J. VOLCKENS Development of a Sampler to Estimate Regional Deposition of Aerosol in the Human Respiratory Tract. Annals of Occupational Hygiene, Nov 2013, 57(9), 1138-1147.

KOULLAPIS, P. G., S. C. KASSINOS, M. P. BIVOLAROVA AND A. K. MELIKOV Particle deposition in a realistic geometry of the human conducting, airways: Effects of inlet velocity profile, inhalation flowrate and electrostatic charge. Journal of Biomechanics, Jul 2016, 49(11), 2201-2212.

LIZAL, F. Experimentální výzkum transportu a depozice aerosolů v dýchacím traktu člověka. In. Brno: Vysoké učení technické v Brně, Fakulta strojního inženýrství, 2012, p. 137 p.

LIZAL, F., M. BELKA AND J. ELCNER Measurement of fiber deposition in a human lung model by Phase contrst microscopy with automated image analyses Engineering Mechanics, 2013, 20(3/4), 187-194.

LIZAL, F., J. JEDELSKY, J. ADAM, M. BELKA, et al. Application of Positron Emission Tomography to Aerosol Transport Research in a Model of Human Lungs. In *7th International Conference on Experimental Fluid Mechanics (EFM).* Tech Univ Liberec (TU Liberec), Hradec Kralove, CZECH REPUBLIC: EDP Sciences, 2012, vol. 45.

MATIDA, E. A., W. H. FINLAY, C. F. LANGE AND B. GRGIC Improved numerical simulation of aerosol deposition in an idealized mouth-throat. Journal of Aerosol Science, Jan 2004, 35(1), 1-19.

NAHAR, K., N. GUPTA, R. GAUVIN, S. ABSAR, et al. In vitro, in vivo and ex vivo models for studying particle deposition and drug absorption of inhaled pharmaceuticals. European Journal of Pharmaceutical Sciences, Aug 2013, 49(5), 805-818.

NEWMAN, S. P. AND I. R. WILDING Imaging techniques for assessing drug delivery in man. Pharmaceutical Science & Technology Today, May 1999, 2(5), 181-189.
OLLINGER, J. M. AND J. A. FESSLER Positron-emission tomography. Ieee Signal Processing Magazine, Jan 1997, 14(1), 43-55.

PARK, C. W., Y. S. RHEE, F. G. VOGT, D. HAYES, et al. Advances in microscopy and complementary imaging techniques to assess the fate of drugs ex vivo in respiratory drug delivery An invited paper.

Advanced Drug Delivery Reviews, Mar 2012, 64(4), 344-356.

PHILLIPS. PET scanner. 2008. Available at: < http://petinfohub.net/gemini-tf-pet-ct >. Accessed on: 20.2.2017.

RESEARCHGATE. Diagram of Spect imaging. 2004. Avaialble at: < https://www.researchgate.net/figure/268746516_fig1_Figure-1-A-schematic-diagram-of-SPECT-Imaging >. Accessed on: 20.2.2017

ROSTAMI, A. A. Computational Modeling of Aerosol Deposition in Respiratory Tract: A Review. Inhalation Toxicology, 2009, 21(4), 262-290.

SCHEUCH, G., W. BENNETT, L. BORGSTROM, A. CLARK, et al. Deposition, Imaging, and Clearance: What Remains to be Done? Journal of Aerosol Medicine and Pulmonary Drug Delivery, Dec 2010, 23, S39-S57.

SCIELO. SPECT data acquisition. 2005. Avaialble at: < http://www.scielo.br/scielo.php?script=sci_arttext&pid=S1807-03022006000200006 >. Accessed on: 20.02.2017

SIEMENS. Magnetic resonance. 2010. Avaialble at: < https://usa.healthcare.siemens.com/magnetic-resonance-imaging/3t-mri-scanner/magnetom-skyra >. Accessed on: 25.2.2017.

THOMPSON, R. B. AND W. H. FINLAY Using MRI to Measure Aerosol Deposition. Journal of Aerosol Medicine and Pulmonary Drug Delivery, Apr 2012, 25(2), 55-62.

VENEGAS, J., T. WINKLER AND R. S. HARRIS Lung Physiology and Aerosol Deposition Imaged with Positron Emission Tomography. Journal of Aerosol Medicine and Pulmonary Drug Delivery, Feb 2013, 26(1), 1-8.

WAGNER, H. N. Hal Anger: Nuclear medicine's quiet genius. Journal of Nuclear Medicine, Nov 2003, 44(11), 26N-+.

WHO. Determination of airborne fibre number concentrations,A recommended method by phase-contrast optical microscopy (membrane filter method),. In. Geneva: World Health Organization (WHO), 1997, p. 53 p.

ZHOU, Y. AND Y. S. CHENG Particle deposition in a cast of human tracheobronchial airways. Aerosol Science and Technology, Jun 2005, 39(6), 492-500.

ZHOU, Y., J. J. SUN AND Y. S. CHENG Comparison of Deposition in the USP and Physical Mouth-Throat Models with Solid and Liquid Particles. Journal of Aerosol Medicine and Pulmonary Drug Delivery, Dec 2011, 24(6), 277-284.

List of abbreviations

CFD	computational fluid and particle dynamics
CT	computed tomography
DD	deposition density
DE	deposition efficiency
DF	deposition fraction
DNS	direct numerical simulation
FLI	fluorescence imaging
Id	model with idealized geometry
LES	large Eddy simulation
MIP	maximum intensity projection
MRI	magnetic resonance imaging
NMR	nuclear magnetic resonance
PCOM	phase contrast optical microscopy
PET	positron emission tomography
R	model with realistic geometry
RANS	Reynolds averaged Navier–Stokes
ROI	region of interest
Seg	segment
SPECT	single photon emission computed tomography
Stk	Stokes number
T	tube segment of idealized model
VOI	volume of interest

List of appendices

Appendix A:
Measured activities for the realistic and idealized geometry

Appendix B:
Deposition characteristics for the idealized and realistic geometry

Appendix C:
Correction factors

Appendix A:
Measured activities for the realistic and idealized geometry

Activity uncorrected (Bq)

Regime\Segment	1	2	3	4	5	6	7	8	9	10	11	12	13	14	15	16
R 60 L/min 1µm	517962	196446	49912	32659	19143	20318	19413	47782	25352	26651	23918	24709	20500	20912	43505	22069
R 15 L/min 1µm	83866	28963	5478	4263	2939	1526	1517	5714	5460	5827	4249	5886	2682	8204	30363	2228
R 15 L/min 1µm	147230	46012	18358	11098	8741	5239	5982	12500	10289	15156	13741	12448	8304	6407	23173	8585
Režim\Segment	**17**	**18**	**19**	**20**	**21**	**22**	**23**	**24**	**25**	**26**	**27**	**28**	**29**	**30**	**31**	**32**
R 60 L/min 1µm	23660	43051	33461	18264	34825	28850	19011	19272	62139	30205	30067	77629	63780	22492	67186	38658
R 15 L/min 1µm	3261	18584	16071	5127	15784	6680	10178	75734	341137	15272	7967	97466	78334	9200	228152	21727
R 15 L/min 1µm	6394	17261	16113	6343	12891	8160	45867	19954	65915	25483	8815	31051	29364	5886	55867	18015

Activity corrected (Bq)

Regime\Segment	1	2	3	4	5	6	7	8	9	10	11	12	13	14	15	16
R 60 L/min 1µm	366398	143741	36909	13127	10928	10892	13434	26474	15517	19265	11417	12866	17969	15448	40059	14474
R 15 L/min 1µm	80125	21241	5683	3970	3216	2167	1792	6218	5900	5192	4294	5169	1966	6522	34524	1540
R 15 L/min 1µm	61012	24316	7703	4605	2544	2911	2581	4907	3738	6302	6526	4960	3983	3582	12100	4396
Regime\Segment	**17**	**18**	**19**	**20**	**21**	**22**	**23**	**24**	**25**	**26**	**27**	**28**	**29**	**30**	**31**	**32**
R 60 L/min 1µm	19709	39230	22094	9037	24418	19803	17434	10794	27264	18210	14628	33419	46812	11542	46443	25430
R 15 L/min 1µm	1961	13109	10616	3558	11099	4373	7654	58379	223431	11564	6381	68484	57799	7317	171850	17737
R 15 L/min 1µm	3575	8936	7937	2730	6305	4191	23420	9020	33995	11865	4115	14958	13518	2284	25325	7926

	Activity uncorrected (Bq)												
Regime\Segment	**Seg 1**	**T1**	**Seg 2**	**T2**	**Seg 3**	**T3**	**T4**	**Seg 4**	**Seg 5**	**T6**	**T5**	**T7**	**T8**
Id 60 L/min 1µm	84238	51526	23148	10080	8675	1712	2115	6871	6806	2504	2121	4189	2875
Id 15 L/min 1µm	170821	53815	17490	12292	6575	2051	1902	3556	4953	1617	1700	1647	3193
Regime\Segment	**T9**	**Seg 6**	**T10**	**Seg 7**	**T11**	**T12**	**T13**	**Seg 8**	**T14**	**T15**	**Seg 9**	**T16**	**T17**
Id 60 L/min 1µm	7375	13568	5471	6801	2426	4029	6464	15079	4339	3388	10738	4189	2626
Id 15 L/min 1µm	5430	14579	12044	7088	1896	2245	7132	20892	3824	4944	11813	4375	3869
Regime\Segment	**T18**	**FiltrT5**	**FiltrT6**	**FiltrT7**	**FiltrT8**	**FiltrT11**	**FiltrT12**	**FiltrT14**	**FiltrT16**	**FiltrT17**	**FiltrT18**		
Id 60 L/min 1µm	3658	11798	12732	14642	26223	21338	25530	23364	24392	19271	22141		
Id 15 L/min 1µm	3201	10796	13036	15242	25140	22683	22708	26917	16900	18678	22195		

	Activity corrected (Bq)												
Regime\Segment	**Seg 1**	**T1**	**Seg 2**	**T2**	**Seg 3**	**T3**	**T4**	**Seg 4**	**Seg 5**	**T6**	**T5**	**T7**	**T8**
Id 60 L/min 1µm	185456	113438	50961	22193	19099	3769	4657	15127	14983	5513	4669	9222	6329
Id 15 L/min 1µm	261320	82327	26756	18804	10058	3137	2909	5441	7578	2473	2601	2519	4885
Regime\Segment	**T9**	**Seg 6**	**T10**	**Seg 7**	**T11**	**T12**	**T13**	**Seg 8**	**T14**	**T15**	**Seg 9**	**T16**	**T17**
Id 60 L/min 1µm	16237	29870	12045	14973	5341	8870	14230	33197	9553	7460	23641	9222	5782
Id 15 L/min 1µm	8307	22303	18424	10844	2901	3435	10911	31961	5850	7564	18072	6693	5919
Regime\Segment	**T18**	**FiltrT5**	**FiltrT6**	**FiltrT7**	**FiltrT8**	**FiltrT11**	**FiltrT12**	**FiltrT14**	**FiltrT16**	**FiltrT17**	**FiltrT18**		
Id 60 L/min 1µm	8053	25975	28030	32235	57733	46977	56206	51438	53700	42428	1243		
Id 15 L/min 1µm	4897	16515	19942	23317	38460	34700	34738	41177	25854	28574	70		

Appendix B:
Deposition characteristics for the idealized and realistic geometry

Deposition efficiency (%)

Regime\Segment	1	2	3	4	5	6	7	8	9	10	11	12	13	14	15	16	17	18	19	20	21	22
R 60 L/min 1µm	6.0	2.5	0.7	0.8	0.7	1.1	2.2	0.7	1.2	0.7	0.9	0.9	9.6	9.8	5.0	3.6	2.8	4.6	3.0	1.7	4.8	4.0
R 15 L/min 1µm	0.8	0.2	0.1	0.2	0.1	0.1	0.3	0.1	0.2	0.1	0.3	0.2	0.6	1.4	2.9	0.6	0.5	0.6	0.7	0.3	1.0	0.4
R 15 L/min 1µm	0.8	0.3	0.1	0.2	0.1	0.2	0.4	0.1	0.2	0.2	0.4	0.2	1.8	1.3	1.0	1.0	0.5	0.7	0.8	0.3	0.9	0.6

Deposition density (m^{-2})

Regime\Segment	1	2	3	4	5	6	7	8	9	10	11	12	13	14	15	16	17	18	19	20	21	22
R 60 L/min 1µm	3.5	3.9	6.3	2.3	4.9	3.1	5.5	5.1	4.3	6.5	3.1	5.1	2.9	1.6	2.6	2.2	2.2	3.6	1.7	2.5	1.9	3.1
R 15 L/min 1µm	0.5	0.4	0.6	0.4	0.9	0.4	0.5	0.7	1.0	1.1	0.7	1.3	0.2	0.4	1.4	0.1	0.1	0.8	0.5	0.6	0.5	0.4
R 15 L/min 1µm	0.5	0.5	1.1	0.7	0.9	0.7	0.9	0.8	0.8	1.7	1.4	1.6	0.5	0.3	0.6	0.5	0.3	0.7	0.5	0.6	0.4	0.5

Deposition fraction (%)

Regime\Segment	1	2	3	4	5	6	7	8	9	10	11	12	13	14	15	16
R 60 L/min 1µm	6.0	2.4	0.6	0.2	0.2	0.2	0.2	0.4	0.3	0.3	0.2	0.2	0.3	0.3	0.7	0.2
R 15 L/min 1µm	0.8	0.2	0.1	0.0	0.0	0.0	0.0	0.1	0.1	0.1	0.0	0.1	0.0	0.1	0.4	0.0
R 15 L/min 1µm	0.8	0.3	0.1	0.1	0.0	0.0	0.0	0.1	0.0	0.1	0.1	0.1	0.1	0.0	0.2	0.1
Regime\Segment	**17**	**18**	**19**	**20**	**21**	**22**	**23**	**24**	**25**	**26**	**27**	**28**	**29**	**30**	**31**	**32**
R 60 L/min 1µm	0.3	0.6	0.4	0.1	0.4	0.3	2.6	2.5	12.5	6.4	11.4	13.2	11.9	8.8	7.9	7.9
R 15 L/min 1µm	0.0	0.1	0.1	0.0	0.1	0.0	0.1	0.6	2.3	0.1	0.1	0.7	0.6	0.1	1.8	0.2
R 15 L/min 1µm	0.0	0.1	0.1	0.0	0.1	0.1	0.3	0.1	0.5	0.2	0.1	0.2	0.2	0.0	0.3	0.1

	Deposition efficiency (%)													
Regime\Segment	**Seg 1**	**T1**	**Seg 2**	**T2**	**Seg 3**	**T3**	**T4**	**Seg 4**	**Seg 5**	**T6**	**T5**	**T7**	**T8**	**T9**
Id 60 L/min 1µm	1.2	0.7	0.3	0.4	0.3	2.1	0.1	0.3	11.5	8.8	8.8	0.9	0.4	0.2
Id 15 L/min 1µm	2.0	0.6	0.2	0.5	0.2	2.8	0.1	0.1	8.8	6.0	7.0	0.3	0.4	0.1
Regime\Segment	**Seg 6**	**T10**	**Seg 7**	**T11**	**T12**	**T13**	**Seg 8**	**T14**	**T15**	**Seg 9**	**T16**	**T17**	**T18**	
Id 60 L/min 1µm	0.3	0.3	0.4	0.2	0.8	0.3	0.6	0.6	0.3	0.9	0.8	0.4	0.8	
Id 15 L/min 1µm	0.3	0.6	0.4	0.1	0.3	0.2	0.6	0.3	0.3	0.7	0.6	0.4	0.5	

	Deposition density (m-2)													
Regime\Segment	**Seg 1**	**T1**	**Seg 2**	**T2**	**Seg 3**	**T3**	**T4**	**Seg 4**	**Seg 5**	**T6**	**T5**	**T7**	**T8**	**T9**
Id 60 L/min 1µm	0.7	1.1	8.5	1.0	4.4	0.8	1.3	5.7	6.7	1.5	1.0	2.5	1.3	1.6
Id 15 L/min 1µm	1.1	0.9	5.3	1.0	2.8	0.8	1.0	2.4	4.0	0.8	0.6	0.8	1.2	1.0
Regime\Segment	**Seg 6**	**T10**	**Seg 7**	**T11**	**T12**	**T13**	**Seg 8**	**T14**	**T15**	**Seg 9**	**T16**	**T17**	**T18**	
Id 60 L/min 1µm	7.8	1.3	6.3	1.1	2.4	1.3	5.3	2.0	1.5	12.8	3.0	1.5	2.1	
Id 15 L/min 1µm	6.9	2.4	5.4	0.7	1.1	1.2	6.0	1.5	1.8	11.7	2.6	1.9	1.5	

	Deposition fraction (%)												
Regime\Segment	**Seg 1**	**T1**	**Seg 2**	**T2**	**Seg 3**	**T3**	**T4**	**Seg 4**	**Seg 5**	**T6**	**T5**	**T7**	**T8**
Id 60 L/min 1µm	1.2	0.7	0.3	0.1	0.1	0.0	0.0	0.1	0.1	0.0	0.0	0.1	0.0
Id 15 L/min 1µm	2.0	0.6	0.2	0.1	0.1	0.0	0.0	0.0	0.1	0.0	0.0	0.0	0.0
Regime\Segment	**T9**	**Seg 6**	**T10**	**Seg 7**	**T11**	**T12**	**T13**	**Seg 8**	**T14**	**T15**	**Seg 9**	**T16**	**T17**
Id 60 L/min 1µm	0.1	0.2	0.1	0.1	0.0	0.1	0.1	0.2	0.1	0.0	0.2	0.1	0.0
Id 15 L/min 1µm	0.1	0.2	0.1	0.1	0.0	0.0	0.1	0.2	0.0	0.1	0.1	0.1	0.0
Regime\Segment	**T18**	**FiltrT5**	**FiltrT6**	**FiltrT7**	**FiltrT8**	**FiltrT11**	**FiltrT12**	**FiltrT14**	**FiltrT16**	**FiltrT17**	**FiltrT18**		
Id 60 L/min 1µm	0.1	3.9	9.6	4.4	19.0	18.3	6.8	10.5	7.6	9.4	6.4		
Id 15 L/min 1µm	0.0	3.1	6.5	4.0	18.1	15.7	7.7	13.8	8.7	10.4	7.4		

Appendix C:
Correction factors of the main analysis (used for calculations) and additional control analysis

Correction factors (-)		
Regime	**Segments**	**Filtr**
R 60 L/min 1µm	1.2	1.1
R 15 L/min 1µm	1.1	1.1
R 15 L/min 1µm	1.0	1.0
Id 60 L/min 1µm	2.2	1.1
Id 15 L/min 1µm	1.5	1.1

CONTROL Correction factors (-)		
Regime	**Segments**	**Filtr**
R 60 L/min 1µm	1.4	1.1
R 15 L/min 1µm	1.2	1.0
R 15 L/min 1µm	1.2	1.1
Id 60 L/min 1µm	2.3	1.1
Id 15 L/min 1µm	1.5	1.1